Electronic Supplementary Information

Tailoring the morphology of Ni-Pt nanocatalysts through the variation of Oleylamine and Oleic acid: *a study on oxygen reduction from synthesis to fuel cell application.*

J.L. Reyes-Rodríguez [a,*], A. Velázquez-Osorio [a], D. Bahena-Uribe [b], A.B. Soto-Guzmán [c], M.A. Leyva [a], A. Rodríguez-Castellanos [a], S. Citalán-Cigarroa [a], and O. Solorza-Feria [a].

[a] Departamento de Química, Centro de Investigación y de Estudios Avanzados del I.P.N. (CINVESTAV). Av. I.P.N. 2508, Col. Zacatenco, Delegación Gustavo A. Madero, C.P. 07360, Ciudad de México, México.

[b] Laboratorio Avanzado de Nanoscopía Electrónica (LANE), CINVESTAV.

[c] Departamento de Física, CINVESTAV.

* Corresponding author: Tel: +52 (55) 5747 3715; Fax: +52 55 5747 3389;

E-mail address: jreyes@cinvestav.mx (J.L. Reyes-Rodríguez).

Table of content

SI-1. Supplementary figures for the Introductory section

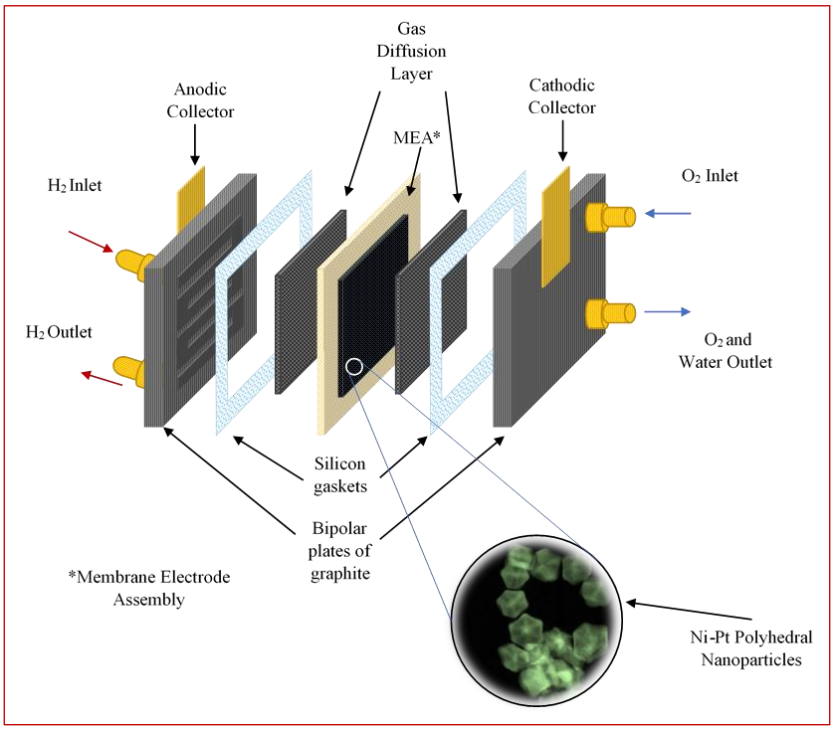

Figure S1. Representation of the main components of a single PEM Fuel Cell.

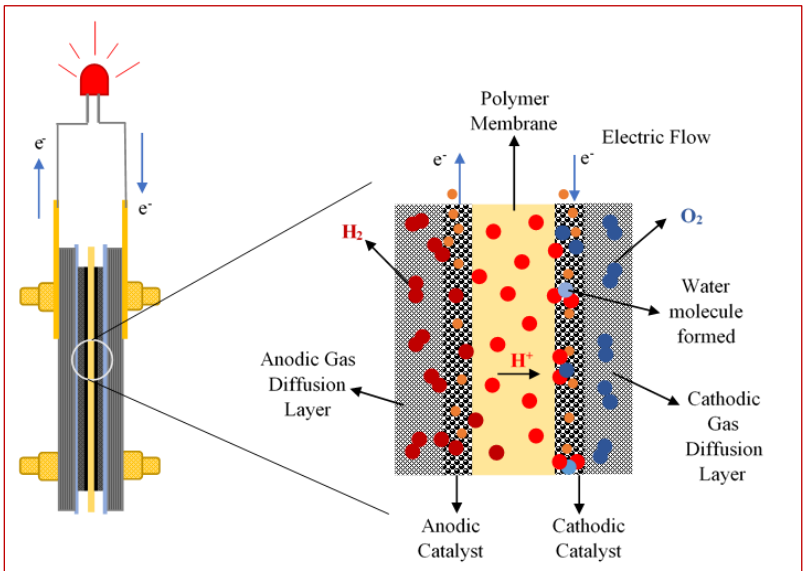

Anodic reaction: $2H_2 \rightarrow 4H^+ + 4e^-$ $E^\circ = 0.0\ V/NHE$

Cathodic reaction: $O_2 + 4H^+ + 4e^- \rightarrow 2H_2O$ $E^\circ = 1.23\ V/NHE$

Global reaction: $2H_2 + O_2 \rightarrow 2H_2O + Heat$ $E^\circ_{cell} = 1.23\ V/NHE$

$$E^\circ_{cell} = E^\circ_{reduction} - E^\circ_{oxidation}$$

Figure S2. Representation of the reactions involved in a single PEM Fuel Cell.

SI-2. Materials, methods, and detailed synthesis procedures

1. Chemicals and material supplies

Nickel (II) nitrate hexahydrate ($Ni(NO_3)_2 \cdot 6H_2O$, 98%), hexachloroplatinic acid hexahydrate ($H_2PtCl_6 \cdot 6H_2O$, ≥37.50% Pt basis), oleylamine (*Oam*, technical grade, 70%), oleic acid (*Oac*, technical grade, 90%) (***Fig. S3***), perchloric acid ($HClO_4$, 70%), 2-propanol (*2POH*, $(CH_3)_2CHOH$, 99.5%), 1-butanol (*BOH*, $CH_3(CH_2)_3OH$, 99.4%), and Nafion® perfluorinated resin solution (5 wt.% in lower aliphatic alcohols and water) were purchased from Sigma-Aldrich.

Vulcan carbon XC-72R (Cabot Co.) (BET surface area: 222 ± 2.4 $m^2\ g^{-1}$ was used as support material for the synthetized catalysts.

Hexane (analytical reagent, 99.5%), acetone (analytical reagent, 99%), and ethanol (analytical reagent, 98.5%) were purchased from Conquimex. These solvents were used as received and without further purification for the washing of the nanomaterials.

Deionized water (18 MΩ·cm) was obtained from an ultra-pure Simplicity® MilliQ water purification system.

Nitrogen gas (N_2, high-purity), oxygen gas (O_2, high-purity), hydrogen gas (H_2, high-purity), and carbon monoxide gas (CO, high-purity) were purchased from Grupo Infra®.

Nafion™ NR-212 membrane (thickness: 50 µm) was used for Membrane Electrode Assemblies (*MEAs*) fabrication and was purchased from Ion Power store.

Carbon-cloth Gas Diffusion Layers (*GDLs*) (thickness: 356 µm) and Pt on Carbon catalyst (*Pt/C Etek*, 20 wt.% Pt on Vulcan carbon) were purchased from FuelCellsEtc store.

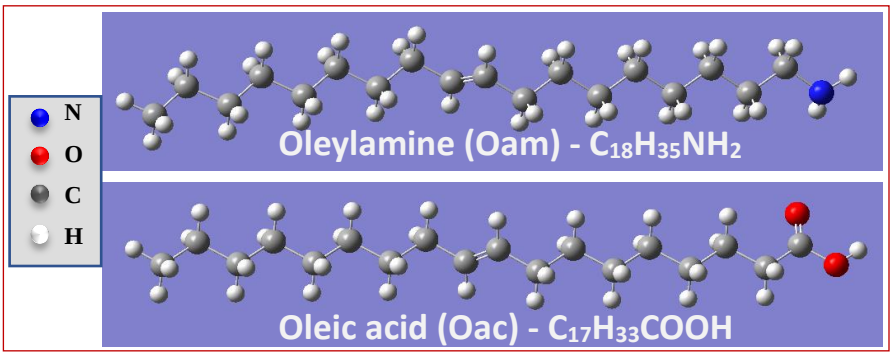

Figure S3. Chemical structure of Oleylamine and Oleic acid.

2. Glassware cleaning

The laboratory glassware materials used underwent strict cleaning to avoid impurities left over from the synthesis which could later form nucleation centers in subsequent experiments. Cleaning involved the use of an alkaline detergent for laboratory material or the use of a homemade soap solution consisting of detergent powder and a spoonful of commercial NaClO (sodium hypochlorite). Glassware was first rinsed with tap water to remove the soap, then with deionized water, and finally with acetone rinses to accelerate drying. The material was dried for a few minutes at 120 °C in an oven. Note: after each synthesis, and especially if seasonally working with other metals in the same glassware, it is recommended to pour *Aqua regia* (mixture of HNO_3: HCl concentrated in 1:3 volume ratio) into the glass materials for a few hours to dissolve any metal traces. Afterwards, glassware should be rinsed with deionized water and washed according to the previous procedure.

3. Synthesis setup.

Figure S4 shows the configuration of the nanoparticles' synthesis setup. A small magnetic stirring hot plate was placed on a manual lift platform inside the fume extraction hood. A heating mantle was placed on the hot plate, its temperature was regulated by a single-phase AC voltage variable transformer. On the heating mantle rested a modified round-bottom flask (250 ml capacity) with a central frosted joint (24/40 connection) and four frosted joints (14/23) around it. A Dean-Stark trap was connected to the flask to collect condensed vapors through a small glass container filled with dried silica gel beads to absorb moisture from the system. The trap was connected to a Graham-style condenser column cooled by cold-water recirculation. This setup was coupled to a vacuum pump to extract the vapors generated during synthesis. The conditions of reduced pressure were regulated by a set of Teflon stopcocks; one was used to allow the entry of air to restore the atmospheric pressure of the system and the other one was connected to a water trap to monitor the exhaust of vapors. A frosted glass stopper was placed on one of the 14/23 joints to allow the addition of reaction agents. Magnetic stirring of the reaction mixture (700-800 rpm) was performed with a small magnetic bar (1.5 cm) placed inside the flask. A glass bubbler placed in another 14/23 joint allowed the supply of a continuous N_2 flow into the reaction mix to maintain an inert atmosphere inside the system. Monitoring of the nitrogen flow was performed with the help of the water trap. Two rubber stoppers were placed in the remaining 14/23 joints. The metal precursors were injected through one of them. A digital thermometer with a stainless-steel thermocouple (introduced through the last rubber stopper) was used to directly sense the temperature of the reaction media. All joint connections were further sealed with Teflon tape. The control of the reaction temperature was performed by varying the heat conduction from the mantle to the flask through manual adjustment of the lift platform. A digital chronometer complemented the system and allowed for time-keeping of each stage of the synthesis. Finally, a digital video camera was used to record the entire synthesis process for later analysis; video footage captured the changes in the color of the reaction mixture inside the flask, as well as, the changes in temperature as a function of time.

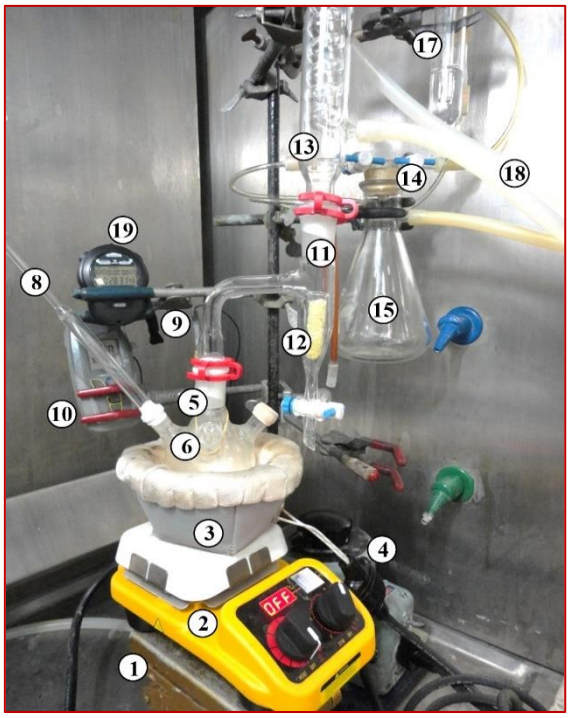

Figure S4. Configuration of the synthesis setup: **1)** manual lift platform, **2)** magnetic stirring hot plate, **3)** heating mantle, **4)** AC voltage variable transformer, **5)** round-bottom flask, **6)** glass stopper for precursors addition, **7)** rubber stopper for injection of metal precursors, **8)** glass bubbler for N_2 supply, **9)** stainless-steel thermocouple probe, **10)** digital thermometer, **11)** Dean-Stark trap, **12)** silica gel beads container, **13)** Graham-type condenser column, **14)** set of Teflon stopcocks, **15)** Kitasato flask used as vapors trap, **16)** connection to vacuum pump, **17)** water trap, **18)** connections to cold-water recirculator, and **19)** digital chronometer.

4. Preliminary procedures

- ***Drying of metal precursors***

The metal precursors can be weighed just before starting the synthesis; however, their hygroscopic nature must be considered, especially in the case of hexachloroplatinic acid. To obtain reproducible results, it is advisable to store the precursor bottles in a desiccator under vacuum. In the case of the Pt precursor, a new reagent bottle was used directly after unpackaging to guarantee that it was in its anhydrous form. In the case of the Ni precursor, the reagent bottle had already been opened, so a few grams of the original precursor were put in a vial and dehumidified in a desiccator under continuous vacuum at room temperature. After 130 hours of drying, the Ni sample for synthesis achieved a constant mass and adopted an appearance of compact flakes of an opaque green color which was different from the emerald-green color that characterizes its wetted form. From the mass balance, it was deduced that it had been possible to pass from the hexahydrate to the tetrahydrate form ($Ni(NO_3)_2 \cdot 4H_2O$) at room temperature without substantially modifying the compound. In this way, the amount of Ni precursor can be weighed more precisely, reducing the errors caused by excessive moisture.

- ***Stock solutions of the metal precursors***

Because numerous experiments were scheduled in order to evaluate the influence of synthesis parameters on the properties of the nanoparticles, and to avoid excessive humidification of the precursors each time the reagents bottles were opened, two stock solutions (25 ml) were prepared according to the following concentrations: 0.777 mM of Ni solution using the dried Ni precursor and 0.418 mM of Pt solution using the recent Pt precursor. Handling of the H_2PtCl_6 should be done with a plastic spoon since Pt can become reduced and deposited on the surface of metallic spatulas. Both solutions were stored in appropriate vials, sealed with Teflon tape, and isolated from light by wrapping the vials in aluminum foil.

- ***Preparation of the Ni-Pt precursor mix***

During synthesis, the metal precursors should be injected all at once with the minimum amount of water possible (fixed at 400 µl) to avoid implosions inside the flask; therefore, a preliminary procedure was implemented by mixing 230 µl of the Ni stock solution and 301 µl of the Pt stock solution ***(Fig. S5-a)*** in a glass vial to form an aqueous metallic precursor mix. The aliquots taken from each metal stock solution ensured that the precise measurement of precursor mass necessary to obtain an estimated content of 30 wt.% Ni and 70 wt.% Pt. The vial was dried under vacuum at room temperature to remove the water from the mixture. After overnight drying, a yellow-green crystalline material was formed ***(Fig. S5-b)***. This procedure was repeated to obtain several vials of the dried Ni-Pt crystals available for re-moistening and use during the synthesis.

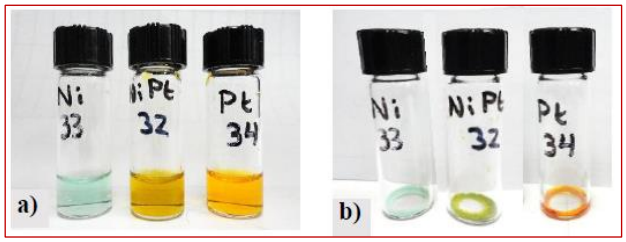

Figure S5. a) Color comparison of the aqueous stock solutions of inorganic Ni and Pt precursors, as well as, the Ni-Pt mixture (shown in the middle); **b)** appearance of the dried crystalline precursors. The dry Ni-Pt material obtained was estimated to have a composition of 30 wt.% Ni and 70 wt.% Pt. This is the metallic mix used for each synthesis.

➢ ***Purification of the organic precursors***

Due to the elevated cost of high-purity Oam and Oac reagents, technical-grade reagents are often used in nanoparticle synthesis. Oam (70%) and Oac (90%) have a pale-yellow color that differs from their pure compounds which are colorless. For these experiments, the organic compounds were distilled under reduced-pressure conditions due to their high boiling points. The distilled compounds were stored under inert conditions and protected from light. Each compound was extracted from its container by volumetric displacement with an N_2 flow before starting each synthesis.

During Oam distillation, aliquots of the head, body, and tail fractions were collected for analysis by mass spectroscopy coupled to HPLC. The mass spectra are shown in ***Figure S6***. It can be observed that purchased Oam presents traces of amine chains from C10 to C20. After distillation process, the body fraction mainly maintains C18 chains in a greater proportion (≈75%), but still retains traces of C14 (≈5%) and C16 (≈19%). The purified body fraction was used for the syntheses of nanoparticles.

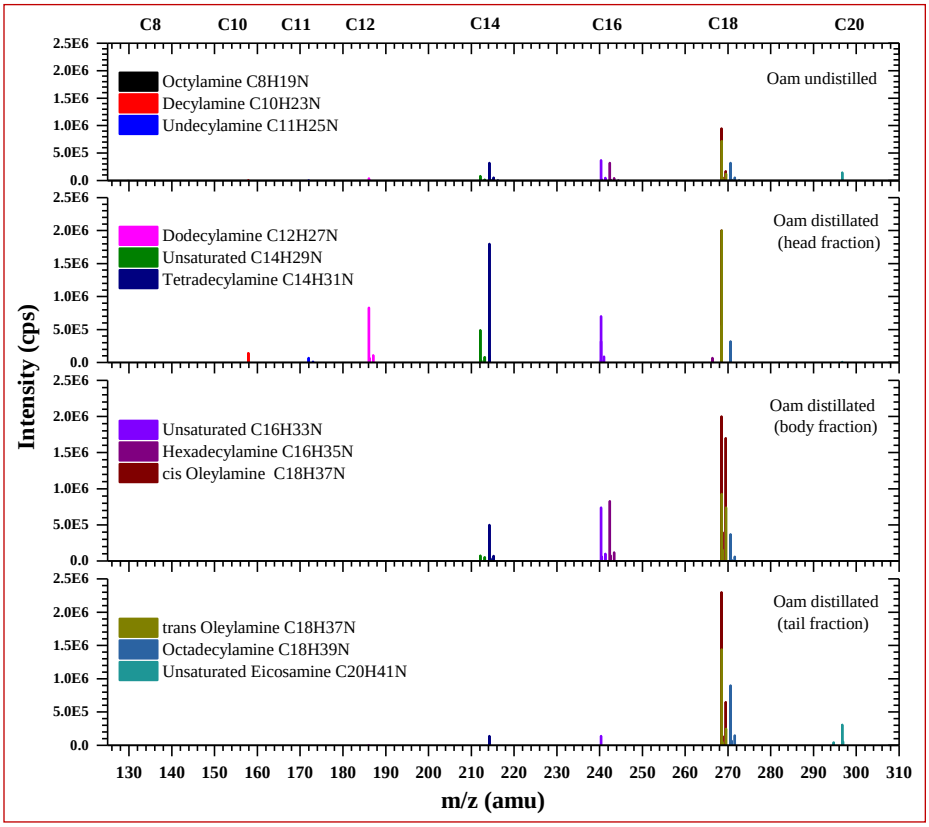

Figure S6. Mass spectra of the fractions collected from de Oam distillation.

Figure S7 shows HAADF-STEM micrographs of two control syntheses of Ni-Pt nanoparticles using undistilled and distilled Oam where it is possible to observe that the use of undistilled Oam produced irregular nanoparticles and with rounded protuberances on their corners (***Fig. 7-a***). Meanwhile, the synthesis using distilled Oam resulted in greater control over particle morphology, leading to the formation of homogeneous polyhedral nanoparticles (***Fig. 7-b***). These observations were taken into account and motivated the use of distilled Oam and Oac for all the Ni-Pt syntheses performed in this study.

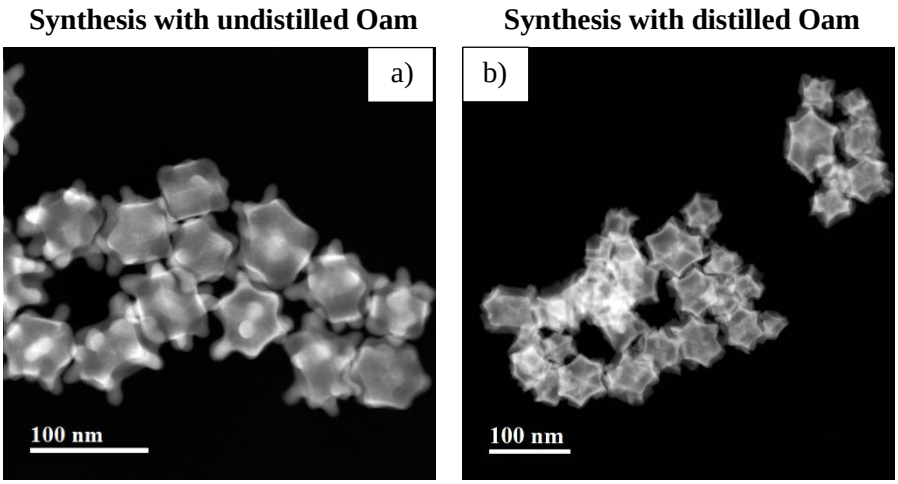

Figure S7. Control syntheses of Ni-Pt nanoparticles using **a)** undistilled Oam and **b)** distilled Oam.

- ***Thermal treatment of Vulcan carbon XC-72R***

Vulcan carbon XC-72R (Cabot Co.) was used as a catalyst support. Some grams of the black powder were put in quartz containers and placed inside a high-temperature treatment tube in a horizontal Carbolite furnace. The thermal treatment was carried out with a heating ramp of 10 °C min^{-1} until reaching 600 °C; this temperature was maintained for 2 hours. A mixed H_2 / N_2 gas flow was supplied to the interior of the tube during the entire thermal treatment process to perform the reduction of organic impurities. The recovered powder was stored for later use and was identified as *VC*.

5. Synthesis of Ni-Pt nanoparticles with Oam:Oac ratio variation

In a typical synthesis, *X* mmol of Oleylamine and/or *Y* mmol of Oleic acid (according to ***Table S1***) were added to the five-neck round-bottom flask and magnetically stirred under a N_2 atmosphere. At the beginning of each synthesis when the amounts of Oam and Oac were mixed at room temperature, it was possible to observe that the temperature increased simultaneously with the addition of Oac. This is attributed of an exothermic acid-base reaction by deprotonation of the Oac to form carboxylate anions ($C_{17}H_{33}COO^-$) and protonated Oam ($C_{18}H_{35}NH_3^+$) to form an acid-base complex, as described in equation ***Ec. 1***.[1] The maximum temperature attained was 60 °C for the NP-Oam50:Oac50 synthesis, where equimolar amounts of Oam and Oac were employed.

$$C_{17}H_{33}COOH + C_{18}H_{35}NH_2 \rightleftharpoons C_{17}H_{33}COO^-:C_{18}H_{35}NH_3^+ \qquad \textit{Ec. S1}$$

After 10 minutes of deoxygenation, the flask was heated to 180 °C (heating stage I). During heating, the evolution of water vapor was observed and displaced by the N_2 flow toward the Dean-Stark trap where the silica gel beads absorbed the moisture and became transparent. On another hand, the dried Ni-Pt crystals in one of the vials previously prepared were dissolved in 400 µl of deionized water. Upon reaching 180 °C, the Ni-Pt precursor solution was injected all at once into de organic mix. This resulted in an immediate formation of dense white vapors which filled the entire flask and are a result of the interaction of the aqueous-organic phases. The precursor injection also resulted in a decrease in temperature to approximately 157 °C which gradually re-establishes itself and the organic-metallic mixture acquires a characteristic pale-green color. The temperature conditions were maintained for five minutes since the moment of injection to ensure

the formation of the metal-ligand complex.[2] Subsequently, reduced-pressure conditions were applied for two minutes to ensure that most of the water injected was extracted from the reaction mixture and condensed in the Dean-Stark trap. Failure to extract the water vapor from the flask causes violent flash-boiling due to the temperature gradient between the organic phase and the precursor solution injected which could also impact synthesis parameter control or, in the worst-case cause the flask to break [2]. Once the vacuum time was ended atmospheric conditions were restored and the AC voltage variable transformer was adjusted to elevate the temperature more rapidly (heating stage II). As the temperature was increased color changes in reaction mixture were observed, ranging from: pale-green (<180 °C), olive green (*ca.*180-190 °C), pale-yellow (*ca.* 200-230 °C), dark yellow (*ca.* 230-250 °C), brown (*ca.* 250-270 °C), and finally black (*ca.* 270-290 °C) as shown in ***Figure S8***. The color-change sequence is in accordance to previous reported work [2]. While the green color indicated the formation of the metal-ligand complex, the black color suggested completion of the chemical reduction process. Finally, the mixture was kept at 270-290 °C (reduction temperature) for an additional 5-10 minutes (reaction time), and then rapidly cooled in a cold-water bath to stop the growth of the nanoparticles. This dark colloidal suspension was re-dispersed by adding hexane, followed by ultrasonic bath.

The bimetallic nanoparticles can be collected by centrifugation (10,000 rpm x 10 min) or by magnetic decantation (in the case of products which possessed magnetic behavior) to facilitate the separation process. Differences in color of the organic supernatant solution, changing from an initial pale yellow to a brown tone, were observed as a function of higher Oac content during synthesis (***Fig. S9***). Materials were subjected to a three-step washing procedure with solvents mixes: *i)* hexane, *ii)* hexane/acetone, and *iii)* acetone/ethanol/deionized water. During every step the solvents were added to the nanoparticles, then the particles were re-dispersed by ultrasonic and/or vortex mixing, and lastly, centrifuged. This procedure guarantees the largest removal of organic matter and precursor remnants from the surface of the nanoparticles. After the last wash, the material was dispersed in acetone through ultrasonic bath. Then, the dispersion was poured into a small beaker, covered with a watch glass, and heated to slowly evaporate the solvent, leaving a film of metallic material. The leftover material was scratched off the beaker and collected with a spatula to obtain powdery flakes with a metallic and glittering appearance.[2]

From the data collected by the video recording, it was possible to obtain the synthesis profile showing the temperature changes as a function of time ***(Figure S10)***. The reduction temperature and the reaction time are the most relevant parameters obtained; by overlapping and comparing the synthesis profiles of two or more similar experiments, it is possible to obtain reliable evidence of reproducibility among the experiments ***(Figure S11)***.

All materials were susceptible to be recovered, with the exception of the N-Oac100 synthesis where it was not possible to precipitate a solid metallic product despite the formation of dark-color precursor mix (***Fig. S9***). Even when the temperature was increased up to 300 °C (***Fig. S11***), it was not possible to precipitate the dispersed product. For the N-Oam100 synthesis, it was noted that the organic-metallic mixture darkens at around 278 °C. If the reaction is stopped and the product recovered, a nickel oxide is obtained (***Fig. S19***). On the other hand, when the reaction is allowed to continue until the temperature reaches ~300 °C, nanoparticles of Ni are obtained. For the synthesis P-Oam100, a gray material with a greasy appearance was obtained; its final weight exceeds by 150-160% the expected metallic product, as is shown in (***Fig. S9***). For the rest of the syntheses, the yields of the metallic product were between 50-60% of the expected value. The glittering appearance and magnetic behavior of metallic powder recovered decreases as the amount of Oac

increases in the synthesis. At an Oac content between 50-100%, the recovered materials lose their paramagnetic behavior even through the parameter of NiPt content used in the syntheses was left unchanged.

Table S1. Performed syntheses of Ni-Pt nanoparticles as a function of the variation in the Oam:Oac ratio.

Label of the material	Oam (mol %)	Oac (mol %)	Oam (mmol)	Oac (mmol)	Metals (wt. %)	Range of reduction temperature (°C)
N–Oam100	100	0	21.3	0	Ni_{100}	278 - 300
P–Oam100	100	0	21.3	0	Pt_{100}	275 - 277
NP–Oam100	100	0	21.3	0	Ni_{30} - Pt_{70}	277 - 279
NP–Oam90:Oac10	90	10	19.2	2.1	Ni_{30} - Pt_{70}	270 - 275
NP–Oam80:Oac20	80	20	17.0	4.3	Ni_{30} - Pt_{70}	265 – 267
NP–Oam70:Oac30	70	30	14.9	6.4	Ni_{30} - Pt_{70}	255 – 258
NP–Oam60:Oac40	60	40	12.8	8.5	Ni_{30} - Pt_{70}	252 – 256
NP–Oam50:Oac50	50	50	10.6	10.6	Ni_{30} - Pt_{70}	249 – 253
NP–Oam30:Oac70	30	70	6.4	14.9	Ni_{30} - Pt_{70}	246 – 250
NP–Oam10:Oac90	10	90	2.1	19.2	Ni_{30} - Pt_{70}	242 – 245
NP–Oac100	0	100	0	21.3	Ni_{30} - Pt_{70}	190 - 193
P–Oac100	0	100	0	21.3	Pt_{100}	173 - 176
N–Oac100	0	100	0	21.3	Ni_{100}	223 - ?

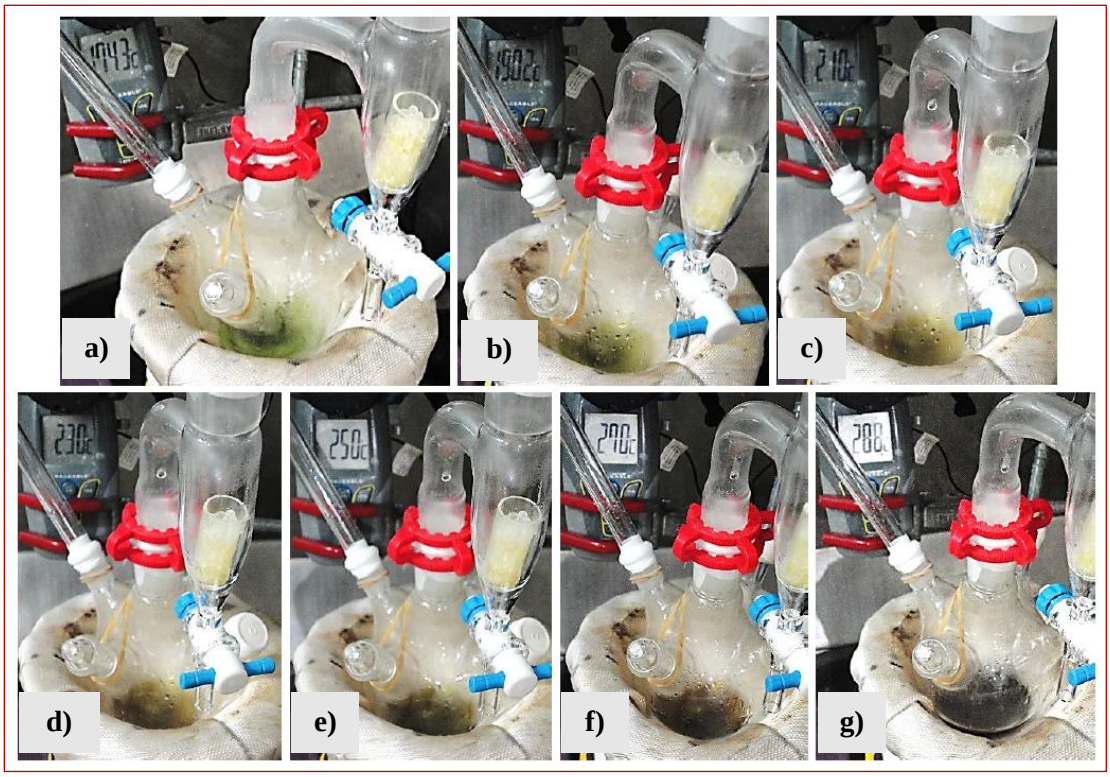

Figure S8. Evolution of Ni-Pt synthesis reaction using Oam. Different color changes in the metal-organic solution were observed as a result of the temperature increase: **a)** pale-green (*ca*. 160-170 °C), **b)** olive green (*ca.* 180 - 190 °C), **c)** pale-yellow (*ca.* 200 - 230 °C), **d)** dark yellow (*ca.* 230 - 250 °C), **e)** brown (*ca.* 250-270 °C), **f)** dark brown (*ca.* 270 - 280 °C), and **g)** black (*ca.* 280 - 290 °C).

Figure S9. Precipitated Ni-Pt products from all performed syntheses with varied Oam:Oac ratios.

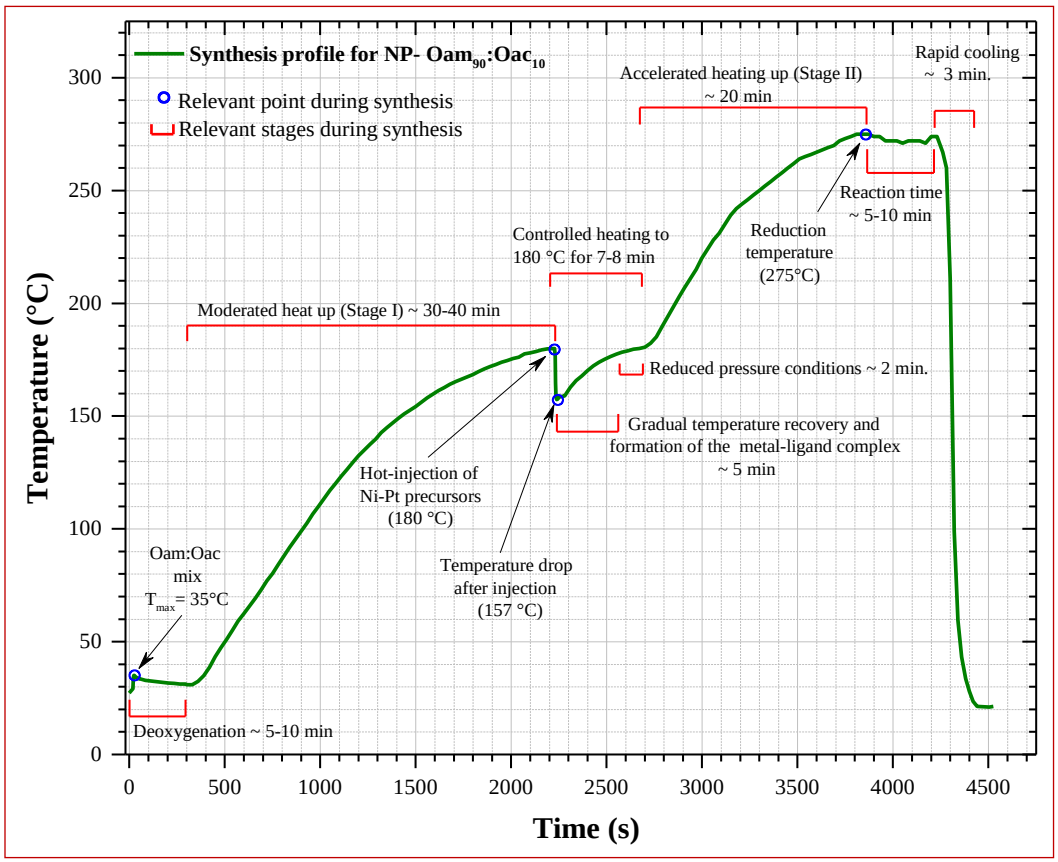

Figure S10. Temperature *vs*. time profile for the NP-Oam90:Oac10 system.

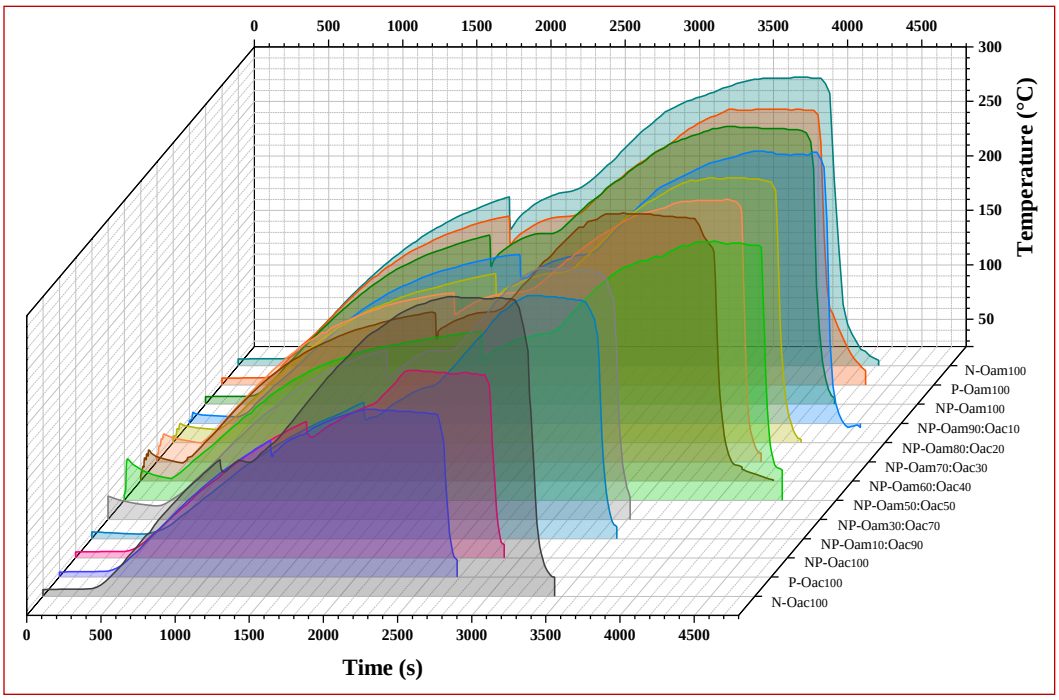

Figure S11. Temperature *vs.* time profiles for all performed syntheses.

6. Dispersion of the Ni-Pt nanomaterials on Vulcan Carbon

The Ni-Pt/VC nanocatalysts were obtained by preparing two separate dispersions. The first one consisted on taking previously synthesized Ni-Pt nanoparticles and dispersing them in 30 ml of 2-propanol with an ultrasonic processor operated in a continuous mode for 30 minutes at an amplitude of 50%. The second dispersion consisted on taking thermally-treated Vulcan carbon powder and dispersing it in 60 ml of 2-propanol with the help of an ultrasound bath for 30 min. Quantities of Ni-Pt and Vulcan carbon were calculated to obtain catalysts at 20 wt.% of Pt. In the case of the N-Oam100 material (without Pt content), dispersion was prepared in carbon at 20 wt.% of Ni. The volumes of solvents used for both dispersions can be optimized depending on the amount of the powders to be suspended. After dispersions were completed, the carbon suspension was kept under mechanical vortex agitation (1500-2000 rpm) while the dispersion of the Pt nanoparticles was added by slow dripping using an addition funnel. The extraction of the solvent in the final suspension was carried out in a rotary evaporator until reaching a semi-dry state. Afterwards, the product was recovered from the flask by adding a small amount of acetone and transferring the mixture to a beaker placed on a hot plate set at 60 °C; this is where the evaporation of the solvent and final drying of the material took place.

SI-3. Physical characterization details

- ***UV-vis spectroscopy***

Aliquots from the precursor mix were taken at 180 °C after the injection of metallic precursor solution during each of the syntheses and rapidly cooled to stop the reaction (***Fig. S12***). From each aliquot, 400 µl were taken and dissolved in ethanol (50/50 $_{v/v}$%) as preparation for UV-vis spectroscopy analysis in a Perkin-Elmer Lambda 2S UV-vis spectrometer with a scan window ranging from 400 to 800 nm and a scan rate of 120 nm min^{-1}.

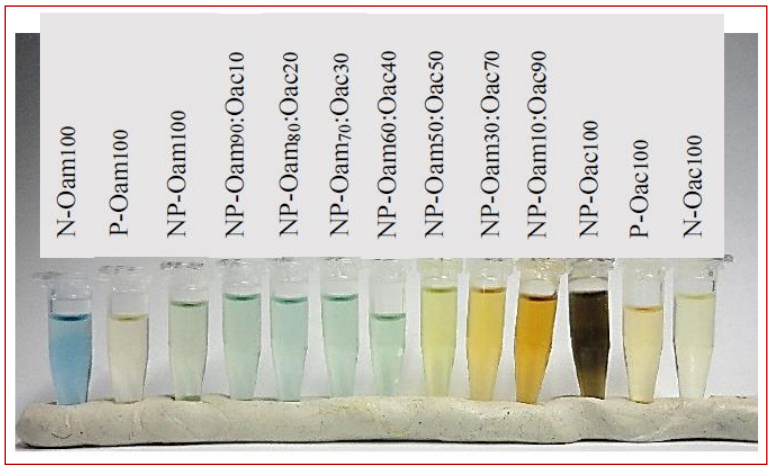

Figure S12. Aliquots extracted from each synthesis (where the Oleylamine (Oam) and Oleic acid (Oac) ratio was varied) for UV-vis and FTIR measurements.

- ***FTIR spectroscopy***

For FTIR measurements, a Varian 640 IR-FTIR spectrometer with an Attenuated Total Reflectance (ATR) configuration in the spectral region of 4000-550 cm^{-1} was employed. The liquid sample (100 µl of each aliquot extracted during syntheses and without dilution) were placed directly above the ATR crystal. Samples of pure Oam and Oac were analyzed as references (***Fig. S13***).

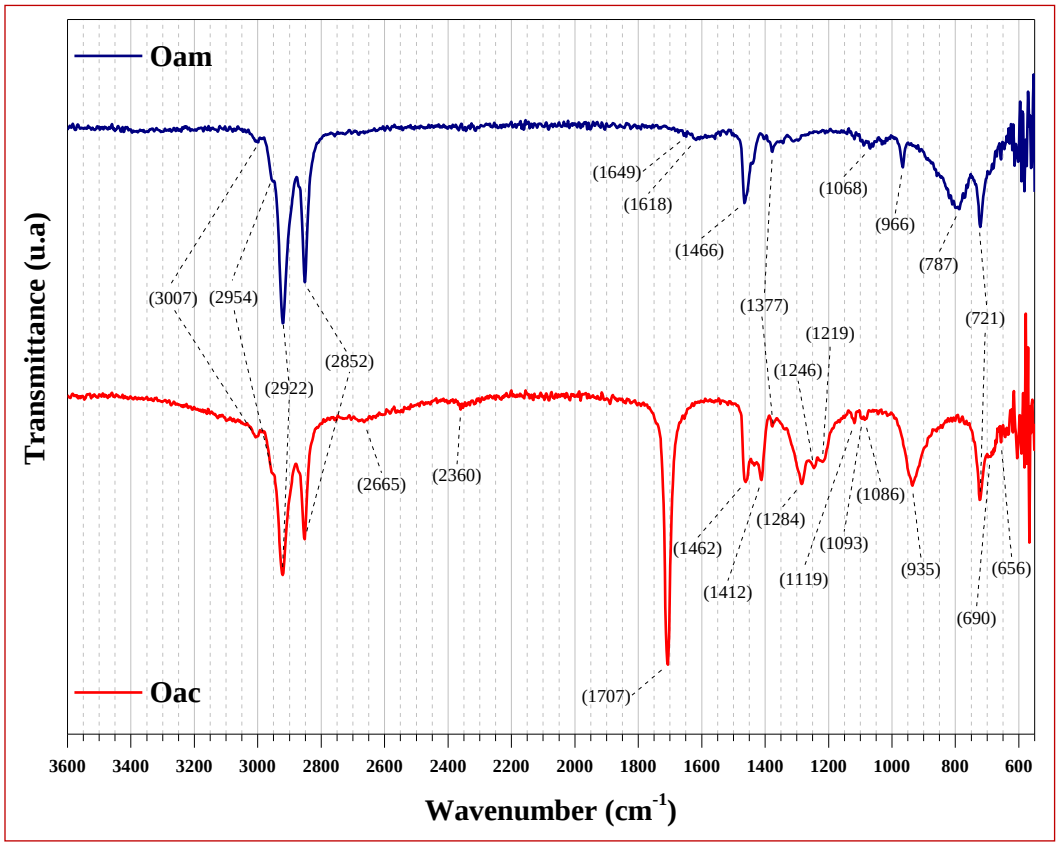

Figure S13. FTIR spectra of pure Oleylamine (Oam) and Oleic acid (Oac).

Table 2. Vibrational modes assignments from FTIR spectra for pure Oam and Oac, and for aliquots extracted from each synthesis.

Functional Group	Vibrational modes[1]	Frequency (cm^{-1})	Assigned in:
NH_4^+	-	3305	NP-Oam_{70}:Oac_{30} NP-Oam_{60}:Oac_{40} NP-Oam_{50}:Oac_{50}
$–CH_2=CH_2–$	ν_s (CH_2)	3007	Oam, Oac
$–CH_3$	ν_{as} ($–CH_3$)	2954	Oam, Oac
$–CH_2–$	ν_{as} ($–CH_2–$)	2922	Oam, Oac
$–CH_2–$	ν_s ($–CH_2–$)	2852	Oam, Oac
–OH	ν (–O–H)	2665	Oac
Environmental CO_2		2360	Oam, Oac
R–COOH	ν (–C=O)	1707	Oac
$–RNH_2$	δ_s ($–NH_2$)	1649	Oam
–RCONH–R’	ν (–C=O)	1631	NP-Oam_{90}:Oac_{10} NP-Oam_{80}:Oac_{20} NP-Oam_{70}:Oac_{30} NP-Oam_{60}:Oac_{40} NP-Oam_{50}:Oac_{50} NP-Oam_{30}:Oac_{70}
R–C=C–R’ trans, di-substituted	ν (–C=C–)	1618	Oam
$R–COO^-$	ν (–C–O)	1614	Product from N-Oac_{100}
–RCONH–R’	δ_{oop} (–NH)	1537	NP-Oam_{90}:Oac_{10} NP-Oam_{80}:Oac_{20} NP-Oam_{70}:Oac_{30} NP-Oam_{60}:Oac_{40} NP-Oam_{50}:Oac_{50} NP-Oam_{30}:Oac_{70}
$–CH_3$ and $–(CH_2)–$	δ_{as} ($–CH_3$) and δ_s ($–CH_2–$)	1466	Oam
$–CH_3$	δ_{as} ($–CH_3$)	1462	Oac
R–COOH	ν (–C–O)	1412	Oac
$–CH_3$	δ_s ($–CH_3$)	1377	Oam, Oac
R–COOH	ν , δ (–COOH)	1284 1246 1219 1119 1093 1086	Oac Oac Oac Oac Oac Oac
$–RNH_2$	ν (–C–N)	1068	Oam
R–C=C–R’ trans, di-substituted	δ_{oop} (–C–H)	966	Oam
R–COOH	δ_{oop} dimer (R–COOH …O–H)	935	Oac
$–RNH_2$	δ_ω ($–NH_2$)	787	Oam
$–(CH_2)–$	δ_ρ ($(–CH_2–)_n$) where n≥4	721	Oam, Oac
R–C=C–R’ cis, di-substituted	δ_{oop} (–C–H)	690	Oac
–OH	δ (–C–OH)	656	Oac

[1] Vibrational modes: ν = stretching, δ = bending. Types: s = scissoring, as = asymmetric, ρ = rocking, ω = wagging, oop = out of the plane.

- ***Electron Microscopy (HAADF-STEM, SEM, and EDS)***

The morphology of the synthesized nanoparticles was characterized through High-Angle Annular Dark-Field Scanning Transmission Electron Microscopy (HAADF-STEM) using a Jeol JEM-ARM 200F microscope equipped with a Schottky-field emission gun operating at 200 keV. Energy Dispersive X-ray (EDS) analysis and Elemental Mapping of Ni and Pt were performed for the synthesis included from N-Oam100 to NP-Oam50:Oac50 which maintained larger particle sizes (> 10 nm). For the other materials, the smaller particle size and agglomeration effect made it difficult to obtain high resolution mapping.

Samples for HAADF-STEM were prepared by dispersing small amounts of each *unsupported Ni-Pt nanomaterial* in 2-propanol; then, 30-40 µl of each suspension was dripped directly onto a lacey carbon-copper grid and allowed to dry at room temperature.

Complementary Scanning Electron Microscopy (SEM) analysis was performed using a field emission Jeol JSM-7401F microscope operated at 2 keV. Quantitative elemental compositions for all materials were obtained by Energy Dispersive X-ray (EDS) analysis during SEM observation using 20 keV. Different regions of the samples were analyzed in order to obtain averaged results.

In order to compare the expected quantitative composition of the synthesis between the measured reagents and those measured by SEM-EDS, *unsupported Ni-Pt* samples for SEM-EDS were prepared by taking 40-50 µl of each one of the suspensions previously prepared for HAADF-STEM and dripped directly onto the surface of small sheets of a conductive copper tape and allowed to dry at room temperature. A sample of pure copper tape was analyzed (***Fig. S14***), observing the presence of S, Al, and Si traces.

For the quantitative compositions used in electrochemical studies, samples for SEM-EDS were prepared by dispersing small amounts of each *supported Ni-Pt/VC nanomaterials* in 2-propanol; then, 40-50 µl of each suspension was dripped directly onto the surface of small Si sheets (placed directly on carbon conductive tape) and allowed to dry at room temperature. With this procedure, it is ensured that the impurities of any other elements are discarded by using sheets of high purity Si; therefore, only the presence of Ni, Pt, and C can be quantified (***Fig. S15***).

Image analysis was performed using the Digital Micrograph (Gatan, Inc.) and ImageJ software. Histograms of particle sizes were obtained through a Gaussian fit of the measured diameters of several nanoparticles. Micrographs of different regions of the sample were taken in order to ensure the calculation of a representative value.

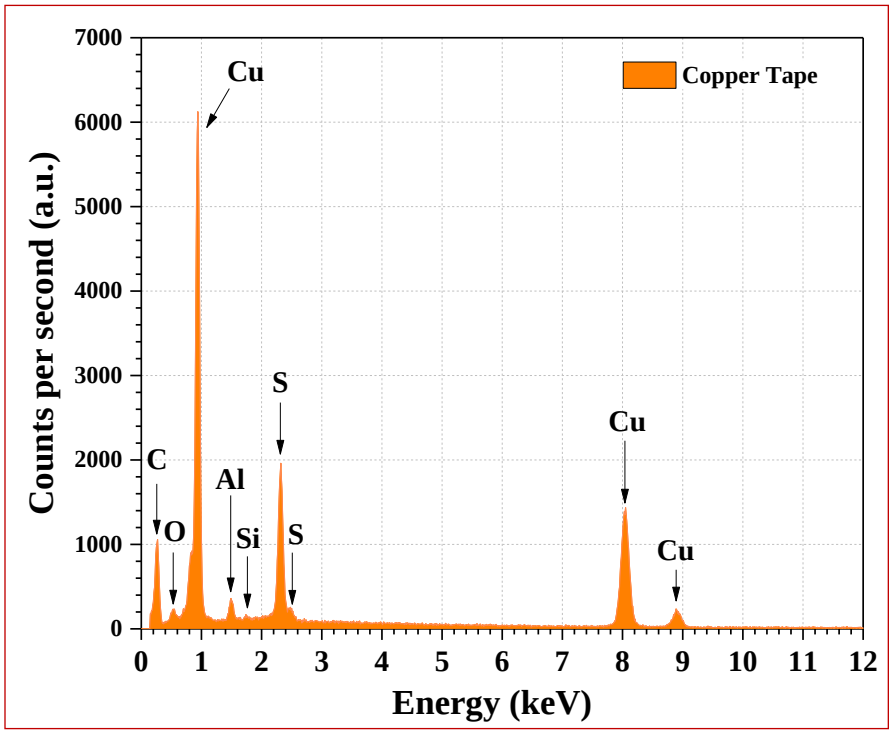

Figure S14. EDS spectrum of copper conductive tape used as support for samples preparation in SEM-EDS characterization.

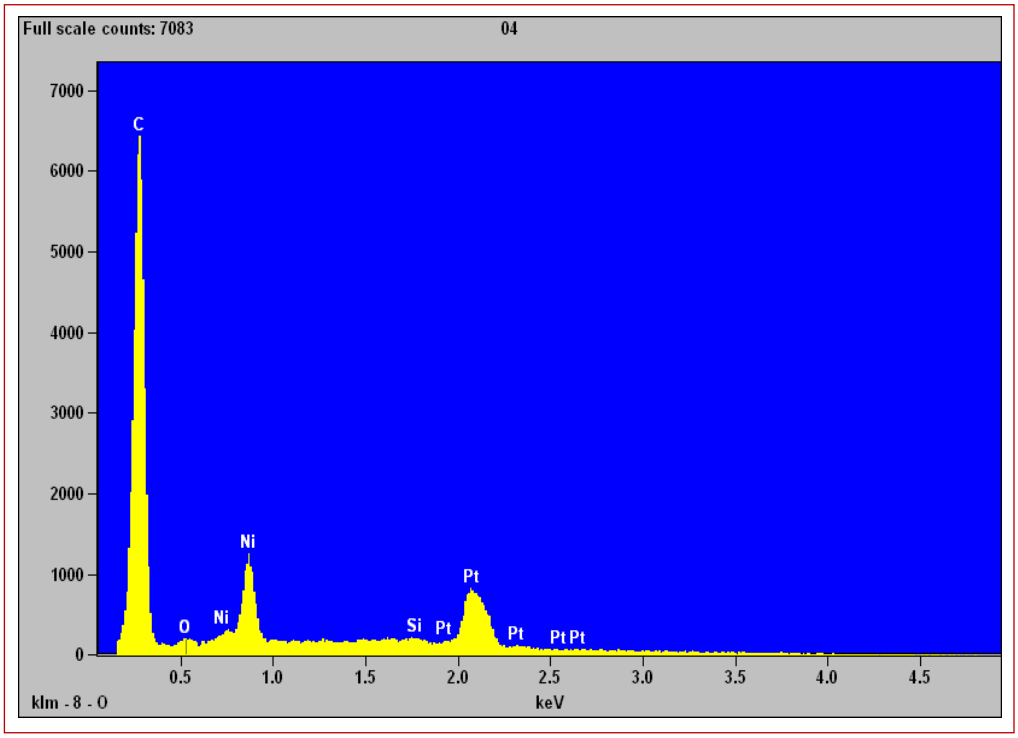

Figure S15. EDS spectrum of the NP-Oam90:Oac10 material using a Si sheet as mount during SEM-EDS characterization. Contributions of Ni, Pt, and C are accurately quantified by this method, avoiding the presence of external impurities as compared to the cases when other mount supports like copper or carbon tape are used.

Additional Figures:

Figure S16 shows High-Angle Annular Bright-Field micrographs of higher magnification, as well as, the particle size distribution histogram of the P-Oam100 material. There is a higher content of organic matter that surrounds the smaller particles, causing them to be held together in the form of clusters. This is consistent with the qualitative characteristics observed during the recovery of the product which possessed a greyish greasy appearance; it is also consistent with the excessive mass obtained where the product yield exceeded 100% of the expected value. This excess mass is consequence of the presence of organic matter. EDS analysis revealed that the composition of the particles was mostly Pt; even through, it was possible to appreciate a small Cl signal inferred to have originated from the Pt precursor (hexachloroplatinic acid).

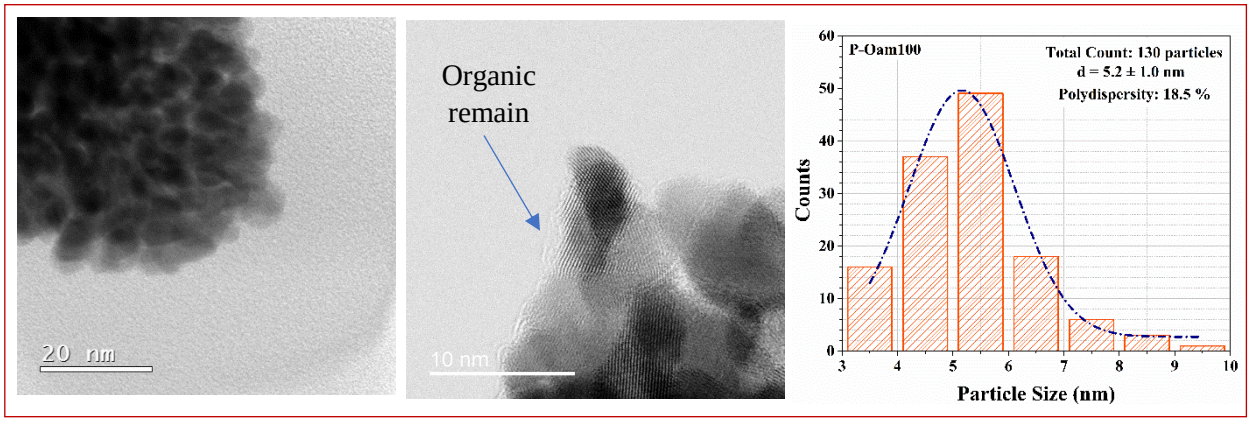

Figure S16. a) High-Angle Annular Bright-Field micrographs of higher magnification of the P-Oam100 material; **b)** Particle size distribution histogram.

Figure S17 shows the HAADF-STEM micrograph of a sample of a commercial Pt/C Etek catalyst for comparative purposes; its corresponding particle size distribution histogram was also obtained (***Fig. S17-b***).

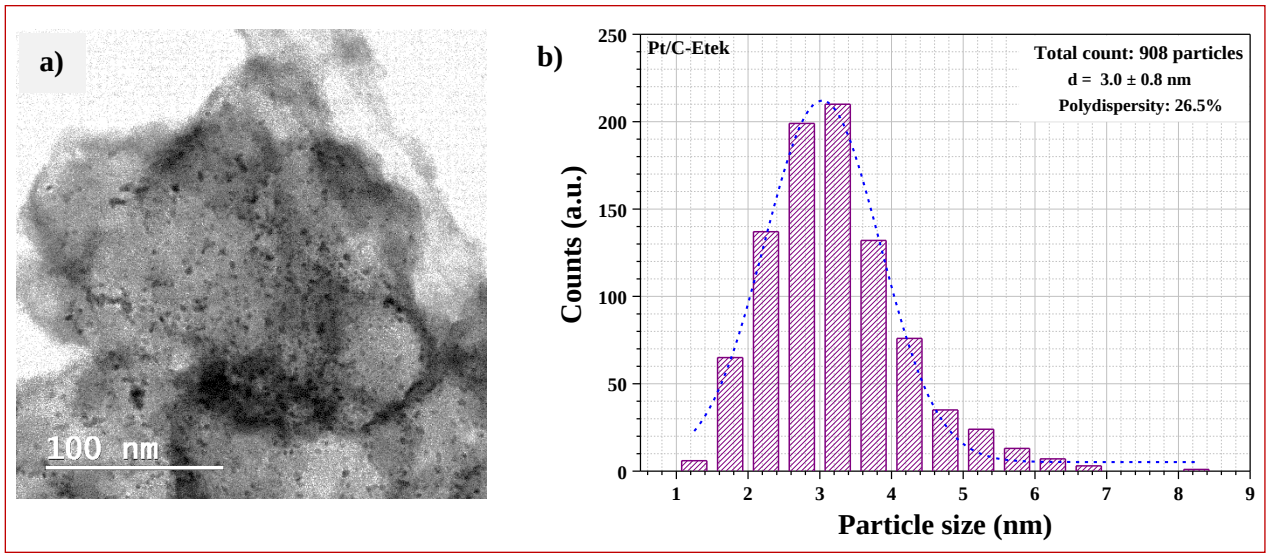

Figure S17. a) High-Angle Annular Bright-Field micrograph of Pt/C Etek catalyst, and **b)** Particle size distribution histogram.

- ***X-ray Diffraction (XRD)***

Phase identification was conducted by X-ray Diffraction using a Bruker D8 Advance Eco diffractometer with a Bragg-Brentano geometric configuration and a Lynxeye detector. The equipment uses a Cu-Kα radiation (λ=1.5418 Å) X-ray source operated to 40 kV and 25 mA. The finely ground powder of each supported material was placed in the most suitable sample holder for the measurement, either a glass holder for conventional measurements or a Si (Zero-background) holder when the available sample amount was very small and when it was essential to eliminate the contribution of the holder's background. In general, the measurement conditions were: a beam aperture grid of 0.6 mm, an analysis window in the range 2θ: 5-130 ° with a step size of 0.01-0.02 °, detection time of 8-10 s, and holder rotation of 20 rpm.

The identification of phases was carried out with the Eva and/or Match 3! software. Numerical data processing was performed using Microsoft Excel and graphics editing was performed with the Origin 9.1 software. Rietveld structural refinement was carried out using the Topas Academic 3.0 software to obtain the corresponding crystal parameters of all supported materials.

Crystallographic charts of the Power Diffraction File (PDF) database and/or from the Crystallography Open Database (COD) where used for identification. The identified phases were: a pure Ni phase matched to PDF 03-065-0380 (whose diffraction maxima are marked with blue circles in main article), an alloy Ni-Pt phase (marked with green diamonds) matched to COD entry # 96-153-8611 (orig. entry: 1538610), and a pure Pt phase matched to PDF 03-065-2868 (marked with red triangles).

From Rietveld refinement the results of crystal phases, lattice parameters, estimated composition, and average crystallite size (by LVol-IB parameter) for each phase present in the materials are shown in ***Table 3*** of main article, the indices for Goodness of Fit (GOF), R values, and degree of crystallinity are shown in ***Table S3***. The deconvoluted X-ray diffractograms of the different crystal phases present for all materials are shown in ***Fig. S18***. The calculated diffractograms obtained from experimental data (diffractograms in dark blue color) are denoted in a light blue line are; the difference between calculated and experimental diffractograms is shown in red. In all cases, fittings of X-ray diffractograms had GOF values less than 2 ($\chi^2 < 2$) which were calculated from R_{exp}, R_{wp}, and R_p values, between 1.00-2.89, suggesting adequate refinements.

Table S3. Indices for Goodness of Fit (GOF) and R values obtained from Rietveld refinements.

Material	GOF	Rexp	Rwp	Rp	Phases	R-Bragg	Sample displacement (mm)	Degree of Crystallinity (%)
N-Oam100	1.19	1.06	1.27	1.00	Ni Cub. Ni Hex.	0.085 0.338	0.4210 (88)	21.49
P-Oam100	1.33	2.52	3.36	2.60	Pt	0.386	0.1200 (78)	43.39
NP-Oam100	1.66	1.61	2.10	1.66	Ni 0.10 – Pt 0.90 Pt Ni	0.445 0.282 0.304	-0.301 (28)	82.27
NP-Oam90:Oac10	1.29	1.75	2.25	1.76	Ni 0.23 – Pt 0.77 Pt Ni	0.125 0.136 0.096	-0.520 (19)	46.57
NP-Oam80:Oac20	1.17	1.74	2.03	1.61	Ni 0.14 – Pt 0.86 Pt Ni	0.190 0.087 0.035	-0.484 (22)	40.50
NP-Oam70:Oac30	1.23	1.69	2.08	1.62	Ni 0.07 – Pt 0.93 Pt Ni	0.089 0.086 0.071	-0.523 (31)	48.88
NP-Oam60:Oac40	1.27	1.82	2.30	1.79	Ni 0.64 – Pt 0.36 Pt	0.325 0.095	0.637 (36)	25.54
NP-Oam50:Oac50	1.13	1.66	1.87	1.47	Ni 0.50 – Pt 0.50 Pt	0.121 0.123	0.415 (14)	37.09
NP-Oam30:Oac70	1.15	2.02	2.33	1.82	Ni 0.02 – Pt 0.98	0.310	0.337 (21)	57.79
NP-Oam10:Oac90	1.20	2.09	2.51	1.93	Ni 0.03 – Pt 0.97	0.287	0.460 (21)	61.87
NP-Oac100	1.30	2.17	2.81	2.21	Ni 0.06 – Pt 0.94	0.448	0.564 (27)	61.22
P-Oac100	1.23	2.31	2.85	2.22	Pt	0.424	0.515 (13)	60.79
N-Oac100	-	-	-	-	-	-	-	-
Pt/C Etek	1.25	2.30	2.89	2.24	Pt	0.360	0.167 (99)	63.43

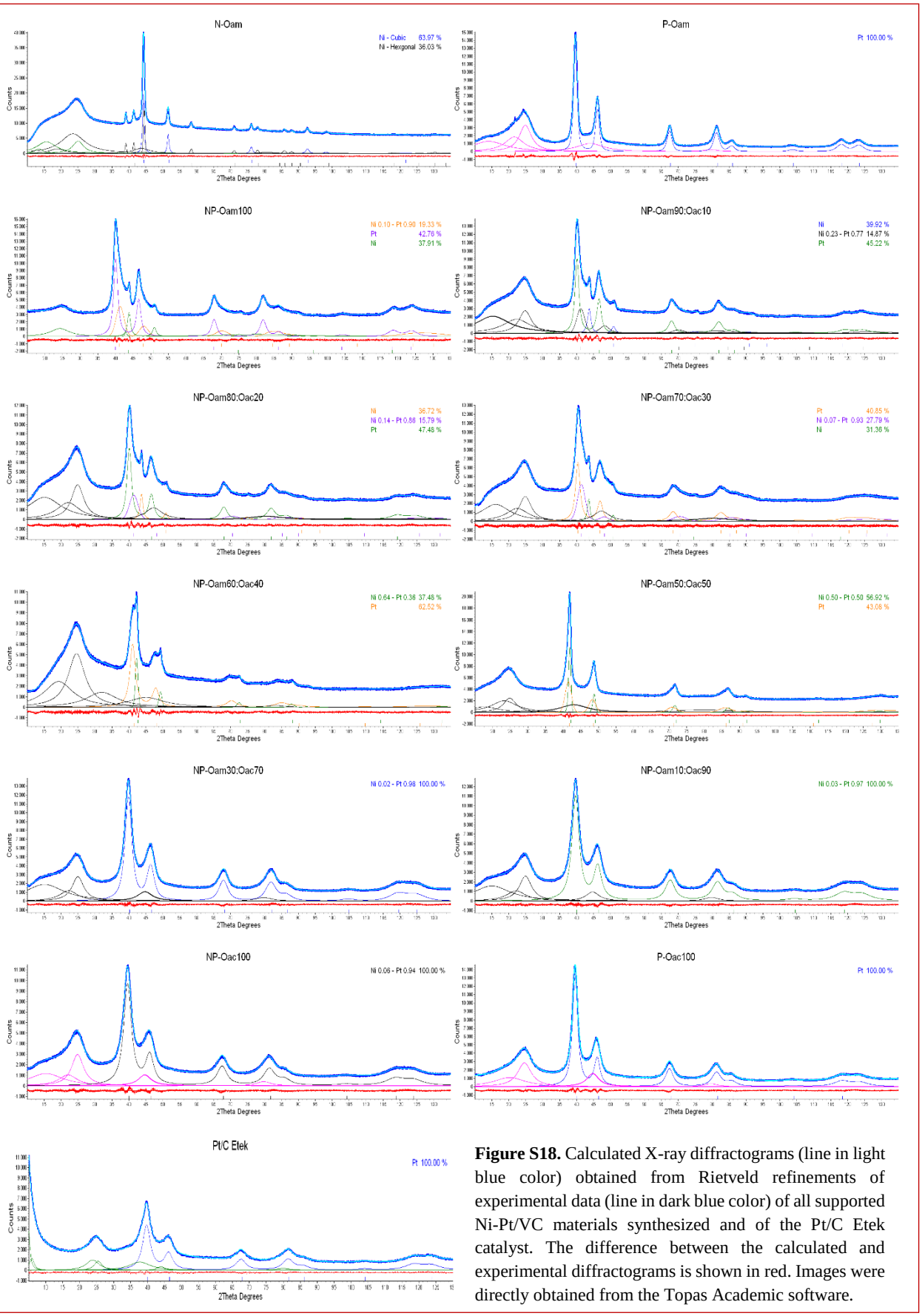

Figure S18. Calculated X-ray diffractograms (line in light blue color) obtained from Rietveld refinements of experimental data (line in dark blue color) of all supported Ni-Pt/VC materials synthesized and of the Pt/C Etek catalyst. The difference between the calculated and experimental diffractograms is shown in red. Images were directly obtained from the Topas Academic software.

Additional Figure:

For the N-Oam100 synthesis using Ni^{2+} precursor and Oam, two different products could be obtained depending on the high temperature used during the synthesis. When the reaction temperature was set at 278 °C, it was possible to observe a change in the color of the metal organic-mixture; this product consisted of a nickel oxide (NiO) compound with a cubic structure (space group Fm-3m) which was matched to PDF 03-065-2901 (marked with brown stars in ***Fig. S19***). However, if the temperature is raised to 300 °C, a black product with paramagnetic behavior was obtained. XRD analysis revealed that this product contained two phases: a dominant (~64%) cubic Ni structure (space group Fm-3m) matched to PDF 03-065-0380 and a hexagonal Ni structure (space group: P63/mmc) matched to PDF 00-045-1027 (marked with orange squares) in a lesser proportion (~36%) (***Fig. S19***). This constitutes important synthesis information because it is possible to control the type of material that is produced solely by controlling the temperature during synthesis.

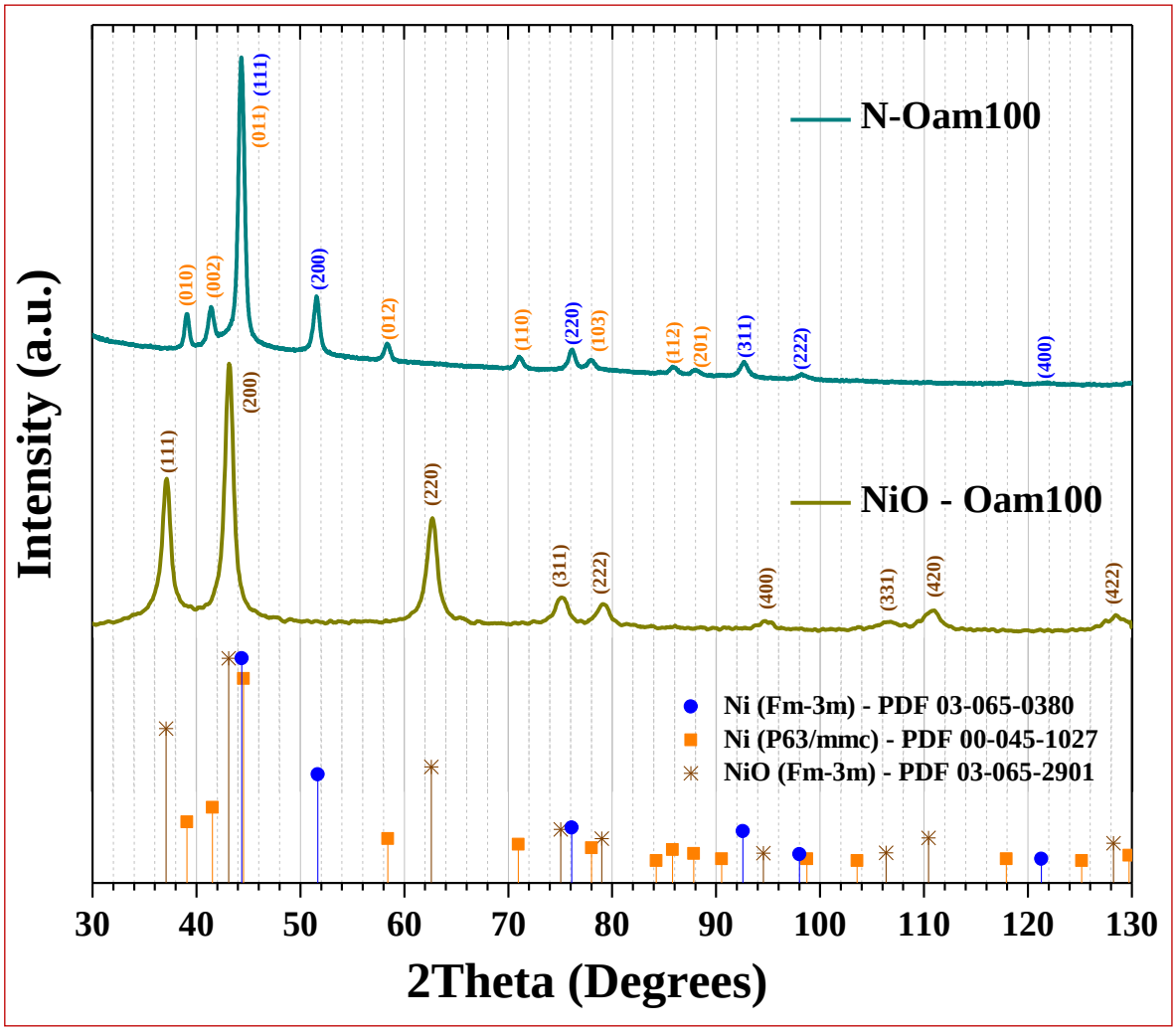

Figure S19. X-ray diffractograms of Ni-based syntheses in Oam; the impact of the synthesis temperature in the obtention of different products occurs as follow: on one hand, there is a formation of mixed Nickel phases with cubic and hexagonal crystalline structures (N-Oam) caused by the reduction at high temperatures (increasing the temperature to ~300 °C after observing the reduction); on the other hand, the production of a single NiO phase (NiO – Oam100) caused by the reduction at lower temperatures (fixing the reduction temperature at ~278 °C).

SI-4. Electrochemical characterization details

- ***Electrochemical configuration***

For the electrochemical evaluation of the catalytic materials, potentiostatic measurements were carried out using an Autolab PGSTAT302N bi-potentiostat controlled with the NOVA 2.1 software interface. The three-electrode electrochemical cell configuration is illustrated in ***Figure S20***. The electrochemical cell consisted of a conical glass piece with ≈30 ml of 0.1 M $HClO_4$ solution as electrolyte. A Pt mesh was used as counter electrode (*C.E.*). The reference electrode (*R.E.*) consisted of a Pt wire inside a glass capillary tube filled with 0.1 M $HClO_4$ electrolyte solution and hydrogen bubbled around it by an electrolysis process. The R.E. is attached to the electrochemical cell through a porous membrane glass bridge which contains the same acid electrolyte solution. The working electrode (*W.E.*) was a homemade Rotating Disk Electrode (RDE) (ohmic resistance: <1.5 Ω) with a flat glassy carbon piece (diameter: 6 mm, circular geometric surface area: 0.283 cm^2) embedded in a Teflon cover. When measurements in bi-potentiostatic mode were required, a commercial Rotating Ring-Disk Electrode (RRDE) (Pine instruments) was used.

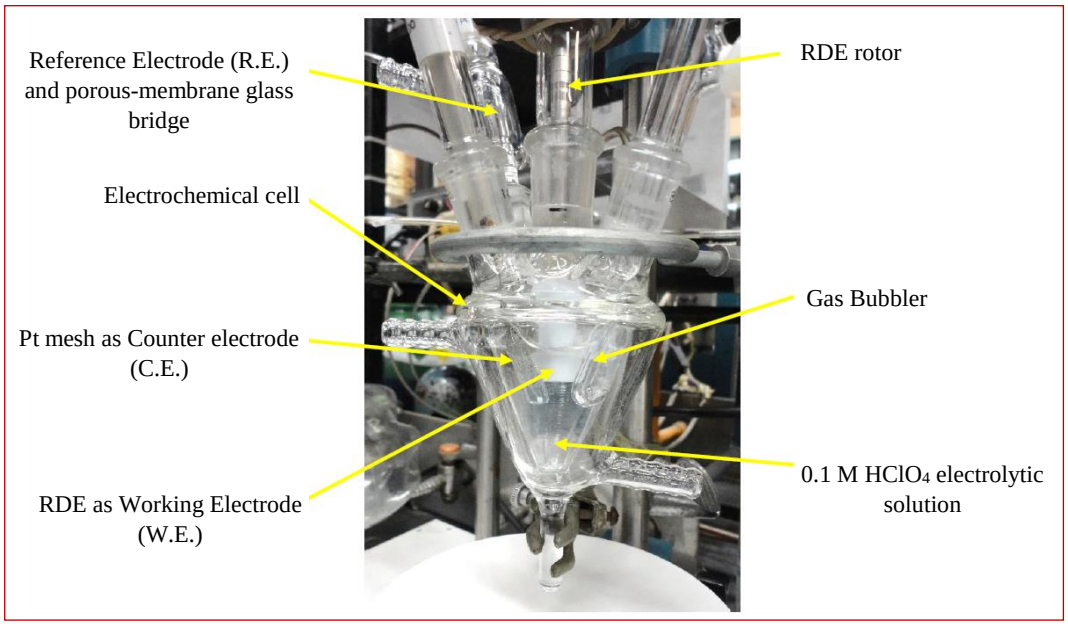

Figure S20. Electrochemical evaluation assembly.

- ***Cleaning protocol for electrochemical material and RDE***

Before carrying out the measurements, the electrochemical cell and all its glass attachments were subjected to rigorous cleaning prevent the presence of any metallic or organic impurities from previous experiments. The cleaning protocol consisted in the addition of a sulfonitric mixture (HNO_3: H_2SO_4, volume ratio 1:1) to the electrochemical cell and letting it act for approximately 2 hours.[3] Afterwards the acid mixture was recovered, and the cell was rinsed and boiled with deionized water *(DI water)* at least three times. Finally, the cell was rinsed two times with the 0.1 M $HClO_4$ electrolyte solution and then, filled with fresh acid electrolyte before the measurements.

The working electrode was cleaned by rinsing it with an ethanol/DI water mixture using an ultrasonic bath. If stains or scratches were noticed on the surface of the glassy carbon, the W.E. was polished to a mirror-finish with a soap-

alumina suspension (alumina grain size: 0.05 µm) on a metallographic pad in a polisher machine. Afterwards, the W.E. was electrochemically cleaned through cyclic voltammetry (*CV*) at different scanning rates until no peaks associated to redox processes were observed.

- ***Catalytic ink preparation***

The preparation of catalytic inks consisted in dispersing a few milligrams (2-5 mg) of the catalytic material in a dispersant solution composed of DI water (74.6 v/v%), Nafion® perfluorinated resin solution (5 wt.% in lower aliphatic alcohols and water, 0.4 v/v%), and 2-propanol (25 v/v%). This formulation is a variation to that commonly found in the literature.[3] A volume of the catalytic ink (10-20 µl) was deposited directly on the surface of the glassy carbon of the W.E., allowing it to dry at room temperature. The catalytic loads (L_{Pt}) were established at 35 µg of Pt cm^{-2}_{geo}. A uniform and homogeneous catalytic film must be obtained during the preparation of the working electrode to achieve good results, either by slightly altering the composition of the components of the dispersing solution or by implementing different ways of drying the electrode. Sometimes, it is simply not possible to get a good film because of the nature of the material itself, but it is important to deposit the best possible film. ***Figure S21*** shows the polished glassy carbon surface of the RDE (***Fig. S21-a***) seen under an optical microscope, as well as, a comparison between two catalytic films: a bad film (***Fig. S21-b***) and a good film (***Fig. S21-c***).

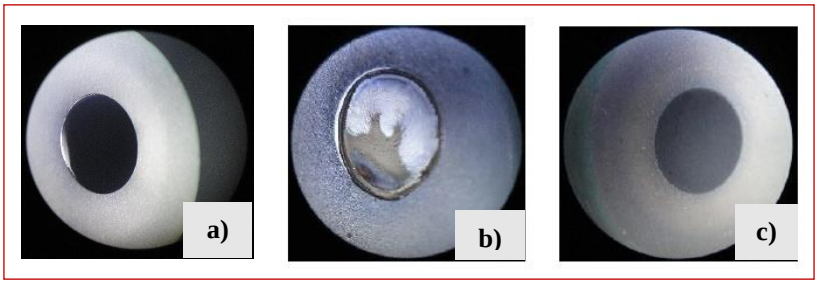

Figure S21. Surface of the RDE and different qualities of catalytic film deposited on the glassy carbon as seen through an optical microscope: **a)** Polished glassy carbon surface of the RDE, **b)** Bad film, and **c)** Good film.

- ***Preparation of the reference electrode (R.E.)***

The preparation of the reference electrode was carried out by applying a potential of -10 V to the Pt wire of the R.E. in contact with the 0.1 M $HClO_4$ electrolyte solution in order to induce electrolysis to form a hydrogen bubble.[3] In this way, a practical and freshly prepared *Reversible Hydrogen Electrode* (*RHE*) (0.0 V) was obtained which offers the advantage allowing the direct analysis of the electrochemical data without the need to correct the reference potentials as is necessary when using other types of reference electrodes.

- ***Electrochemical Measurement Protocols***

Electrochemical measurements consisted in the application of a techniques based on cyclic voltammetry, including as CO stripping and steady-state polarization curves, to comprise a Basic Electrochemical Protocol. Complementary Electrochemical Measurements such as a durability testing based on accelerated electrochemical degradation and the determination of the hydrogen peroxide formed during ORR in RRDE configuration were also performed.

Table S4 shows the summary of the parameters used in the electrochemical measurement protocols. Each electrochemical technique is described in detail in subsequent pages.

Table S4. Parameters used in the Electrochemical Measurements Protocols.

<table>
<tr><th colspan="4">Basic Electrochemical Protocol</th></tr>
<tr><th colspan="2">Cyclic Voltammetry for Activation</th><th colspan="2">Ohmic drop compensation correction</th></tr>
<tr><th>Potential Profile</th><th>Measurement parameters</th><th>Profile</th><th>Measurement parameters</th></tr>
<tr>
<td> 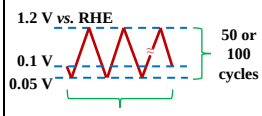

0.1 M HClO₄ under N₂ saturation.</td>
<td>Electrolyte: 0.1 M HClO₄
Temperature: 25-30 °C
Saturation gas: N₂
Potential window: 0.05 – 1.2 V vs. RHE
Scan rate: 50 or 100 mV s⁻¹
EDR rotation rate: 0 rpm
Total potential scans: 100 cycles</td>
<td> 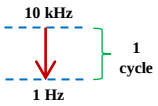

0.1 M HClO₄ under N₂ or O₂ saturation.</td>
<td>Electrolyte: 0.1 M HClO₄
Temperature: 25-30 °C
Saturation gas: N₂ or O₂
Frequency window: 10 kHz - 1 Hz
EDR rotation rate: 0 rpm
Total scans: 1 cycle</td>
</tr>
<tr><th colspan="2">Cyclic Voltammetry</th><th colspan="2">N₂ Background CV</th></tr>
<tr><th>Potential Profile</th><th>Measurement parameters</th><th>Potential Profile</th><th>Measurement parameters</th></tr>
<tr>
<td> 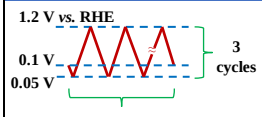

0.1 M HClO₄ under N₂ saturation.</td>
<td>Electrolyte: 0.1 M HClO₄
Temperature: 25-30 °C
Saturation gas: N₂
Potential window: 0.05 – 1.2 V vs. RHE
Scan rate: 20 and 50 mV s⁻¹
EDR rotation rate: 0 rpm
Total potential scans: 3 cycles</td>
<td> 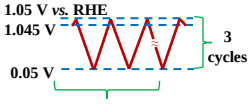

0.1 M HClO₄ under N₂ saturation.</td>
<td>Electrolyte: 0.1 M HClO₄
Temperature: 25-30 °C
Saturation gas: N₂
Potential window: 1.05 – 0.05 V vs. RHE
Scan rate: 20 mV s⁻¹
EDR rotation rate: 0 rpm
Total potential scans: 3 cycles</td>
</tr>
<tr><th colspan="2">CO stripping</th><th colspan="2">Steady-state polarization curves</th></tr>
<tr><th>Potential Profile</th><th>Measurement parameters</th><th>Potential Profile</th><th>Measurement parameters</th></tr>
<tr>
<td> 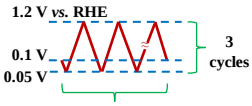

0.1 M HClO₄ under CO saturation by 300 s and then evacuation with N₂ saturation by 600 s.</td>
<td>Electrolyte: 0.1 M HClO₄
Temperature: 25-30 °C
Adsorption potential: 0.1 V vs. RHE
Adsorption gas: CO
Absorption time: 300 s
Saturation gas: N₂
N₂ evacuation time: 600 s
Potential window: 0.05 – 1.2 V vs. RHE
Scan rate: 20 mV s⁻¹
EDR rotation rate: 0 rpm
Total potential scans: 3 cycles</td>
<td> 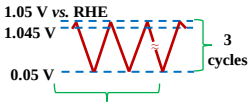

0.1 M HClO₄ under O₂ saturation Rotation rates: 400, 900, 1600, and 2500 rpm.</td>
<td>Electrolyte: 0.1 M HClO₄
Temperature: 25-30 °C
Saturation gas: O₂
Potential window: 1.05 – 0.05 V vs. RHE
Scan rate: 20 mV s⁻¹
EDR rotation rates: 400, 900, 1600, and 2500 rpm
Total potential scans: 3 cycles</td>
</tr>
<tr><th colspan="4">Complementary Electrochemical Measurements</th></tr>
<tr><th colspan="2">Durability test by accelerated electrochemical degradation</th><th colspan="2">Determination of collector factor in RRDE</th></tr>
<tr><th>Potential Profile</th><th>Measurement parameters</th><th>Potential Profile</th><th>Measurement parameters</th></tr>
<tr>
<td> 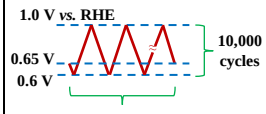

0.1 M HClO₄ under O₂ saturation. Basic Electrochemical Protocol after 1000, 3000, 5000, and 10,000 cycles.</td>
<td>Electrolyte: 0.1 M HClO₄
Temperature: 25-30 °C
Saturation gas: O₂
Potential window: 0.6 – 1.0 V vs. RHE
Scan rate: 100 mV s⁻¹
EDR rotation rate: 0 rpm
Total potential scans: 10,000 cycles, performing the Basic Electrochemical Protocol after: 1000, 3000, 5000, and 10,000 cycles</td>
<td> 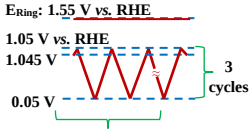

10 mmol of K₃Fe(CN)₆ in 0.1 M HClO₄ under N₂ saturation Rotation rates: 400, 900, 1600, and 2500 rpm.</td>
<td>RRDE configuration
Electrolyte: 10 mmol of K₃Fe(CN)₆ in 0.1 M HClO₄
Temperature: 25-30 °C
Saturation gas: N₂
Potential window: 1.05 – 0.05 V vs. RHE
Fixed potential in Ring: 1.55 V vs. RHE
Scan rate: 20 mV s⁻¹
EDR rotation rates: 400, 900, 1600, and 2500 rpm
Total potential scans: 3 cycles</td>
</tr>
<tr><th colspan="2">Determination of H₂O₂ formation by RRDE</th><td colspan="2" rowspan="2"></td></tr>
<tr><th>Potential Profile</th><th>Measurement parameters</th></tr>
<tr>
<td> 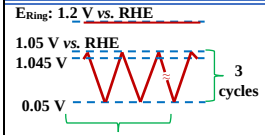

0.1 M HClO₄ under O₂ saturation Rotation rates: 400, 900, 1600, and 2500 rpm</td>
<td>RRDE configuration
Electrolyte: 0.1 M HClO₄
Temperature: 25-30 °C
Saturation gas: N₂
Potential window: 1.05 – 0.05 V vs. RHE
Fixed potential in Ring: 1.2 V vs. RHE
Scan rate: 20 mV s⁻¹
EDR rotation rates: 400, 900, 1600, and 2500 rpm
Total potential scans: 3 cycles</td>
</tr>
</table>

➢ ***Cyclic voltammetry for catalyst activation***

The first electrochemical technique to evaluate the materials was cyclic voltammetry (*CV*) measured over an electroactivity window of 0.05-1.2 V *vs.* RHE with a scan rate of 50 mV s^{-1} under N_2 saturation conditions of the electrolyte. The immersion potential of the W.E. was set at 0.1 V *vs.* RHE to observe possible peaks of oxidation during the first scan which are associated with the oxidation of the non-noble metal or in the case of a deficient Pt. No oxidation peaks (associated to Ni oxidation process) were detected during the first cycle of voltammetry; thus, it was possible to discard the segregation or exposure of free Ni atoms in the Ni-Pt materials. Several potential cycles (approx. 100 sweeps) were performed to activate the catalytic material before taking measurements (***Figure S22***). A considerable number of activation cycles was required for all the synthesized catalysts, this is due to the presence of residual organic matter on the surface of the nanoparticles left over from their synthesis. The criteria established to determine whether a material had achieved activation was by waiting until the cyclic voltammograms of two consecutive cycles overlapped. Once the activation was complete, the electrolyte solution in the cell was rinsed with DI water and fresh electrolyte was added.

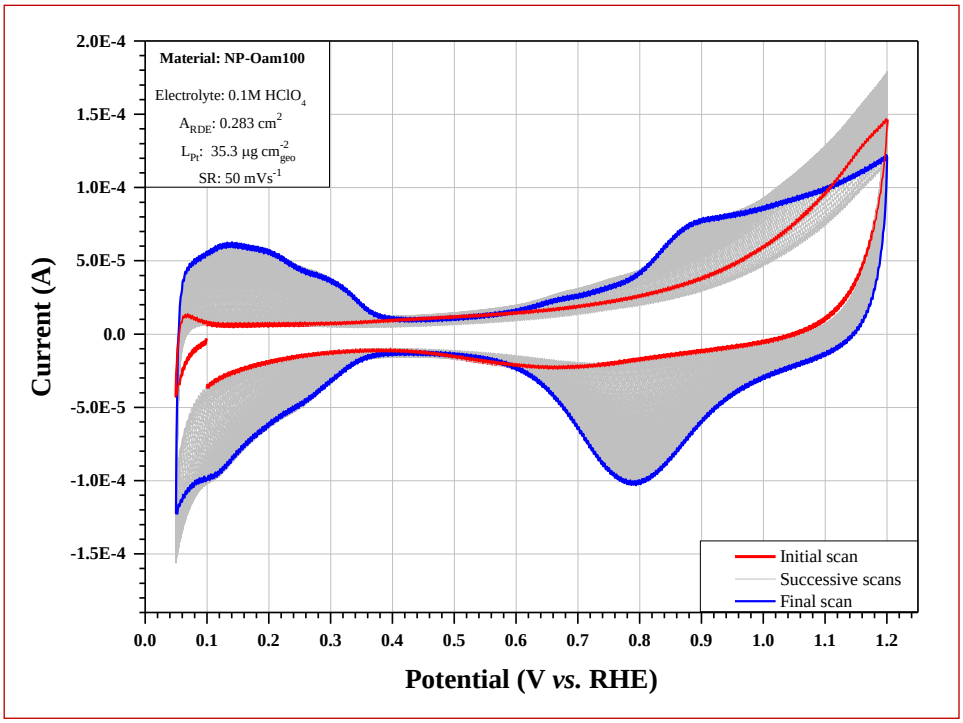

Figure S22. Activation C*V*s of the NP-Oam100 catalyst at 50 mV s^{-1} in 0.1M $HClO_4$ electrolyte solution. The catalytic loading was L_{Pt} = 35.3 µg cm^{-2}_{geo}. One hundred activation cycles were performed.

➢ ***Compensation for Ohmic Drop***

The resistance in the electrolyte solution (R_{soln}) formed between the R.E. and W.E. represents the major contribution to the ohmic drop in electrochemical measurements. Its determination is of significant importance and must be considered in the ohmic drop compensation correction (iR_{soln}) applied during the electrochemical techniques.[4–6] An impedance measurement was performed in the range 10 kHz - 1 Hz for the determination of the R_{soln} corresponding to the value of

the semicircle at high frequencies (***Figure S23***). In all cases, the measurements were corrected using a resistance compensation in the range 17-23 Ω; this is a relatively low value thanks to the physical design of the electrochemical cell.

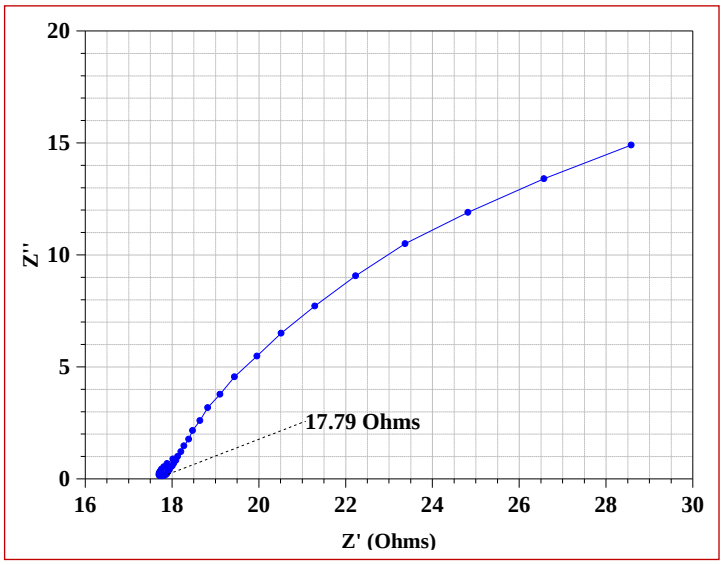

Figure S23. Impedance measurement to determine the resistance of the solution.

- ***Cyclic voltammetry and background measurement for capacitive correction***

After the electrochemical cell was filled with new electrolyte, a new CV measurement was performed following the same parameters as in the catalytic activation procedure. However, this time the measurement was made considering the ohmic drop compensation in order to obtain a final profile which could be used for comparison with other materials, for example, with Pt/C Etek. ***Figure S24*** shows different regions and electrochemical processes taking place in the potential scan window for Pt/C Etek. These regions are: *i)* anodic and cathodic peaks between 0.05 - 0.4 V *vs.* RHE which correspond to the Pt-hydrogen adsorption/desorption region where the cathodic peaks around 0.11 V *vs.* RHE and between 0.23 - 0.33 V *vs.* RHE are mainly associated to the adsorption process of hydrogen atoms on the respective (110) and (100) sites of the polycrystalline Pt nanoparticles,[7–9] *ii)* the capacitive region (0.4 V *vs.* RHE < E < 0.6 V *vs.* RHE) where a double layer charging process is carried out, and *iii)* the Pt-oxide formation/reduction region (E > 0.7 V *vs.* RHE) where the broad anodic peak around 0.8 - 0.9 V *vs.* RHE is associated to the formation of Pt-O and Pt-OH species as a result of oxidation of the Pt surface, and the cathodic peak around 0.76 V *vs.* RHE is associated to the Pt-oxide reduction process.[3,7,10–13]

After the first CV, a second CV was carried out at 20 mV s^{-1} in a window of 1.05 - 0.05 V *vs.* RHE under N_2 saturation conditions to obtain a background profile that would serve to subtract the capacitive effects of the polarization curves when the system was saturated with O_2, as is shown in a later section.

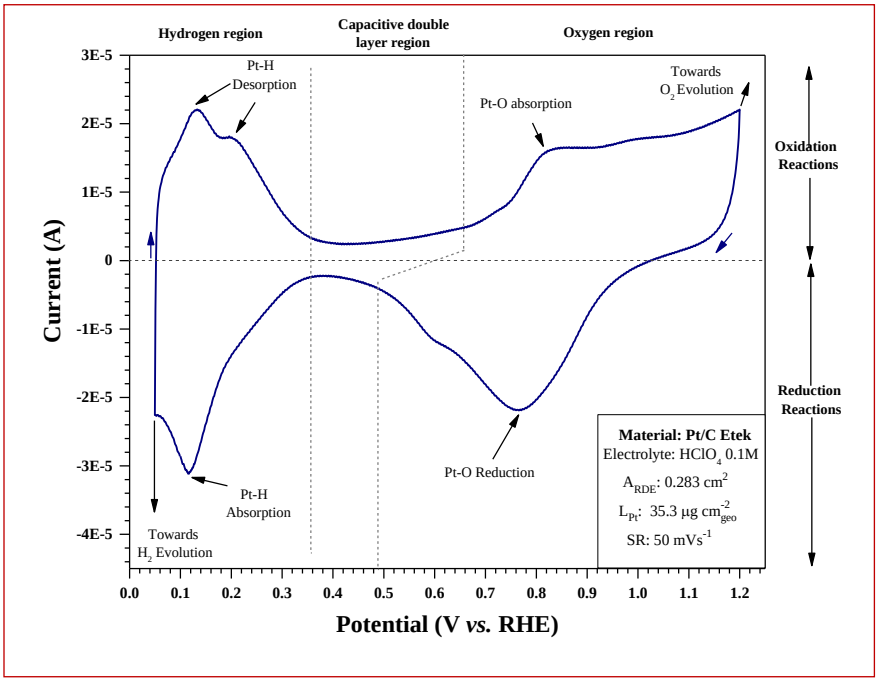

Figure S24. CV obtained after activation for the Pt/C Etek catalyst at 50 mV s^{-1} in a fresh 0.1M $HClO_4$ electrolyte solution. The catalytic loading was L_{Pt} = 35.3 µg cm^{-2}_{geo}.

- ***CO stripping***

The Electrochemical Surface Area (ECSA) measured in m^2 g^{-1} represents the number of electrochemically active sites available per mass of Pt responsible for the catalytic activity. This value may be calculated by two ways: from the determination of the charge of the hydrogen region or through the integration of the anodic peak obtained during the carbon monoxide electrooxidation (CO stripping) technique derived from cyclic voltammetry.[14–17] The last method is currently the most widely used to obtain the real active surface area in the case that noble metals like Pt are used as nanocatalysts, since CO has the property of becoming adsorbed on the surface of Pt through the *poisoning effect.*[18]

CO stripping (***Fig. S25***) was used to determine the ECSA values of all Ni-Pt catalysts under study. Before measurement, the electrochemical cell was refilled with a fresh electrolyte. The electrolyte was saturated by a CO flow for 600 seconds while maintaining an RDE potential of 0.1 V *vs.* RHE. Under these conditions, the CO is adsorbed on the surface of the active metal (Pt). Subsequently, the solution was saturated with an intense N_2 flow to evacuate the remaining CO from the cell. Then, the CV measurement was carried out at 20 mV s^{-1} in a potential window of 0.05 - 1.2 V *vs.* RHE, observing anodic peaks in the range 0.6-0.9 V *vs.* RHE associated to the electro-oxidation process of CO, as it shown in ***Fig. S25***.

Subtraction of cycles 1 and 2 is used to remove the capacitive effects while the integration of the CO oxidation peak (considering the scan rate applied, v) is used to obtain the CO absorption charge (Q_{CO} in µC) as described in equation ***Ec. S2***, in ***Fig. S25***.[10] Subsequently, the Q_{CO} is divided by 420 µC cm^{-2} which corresponds to the adsorption charge for the formation of a CO monolayer on the metallic surface of Pt in polycrystalline electrodes.[17,19] This is calculated to obtain the CO surface (S_{CO} in cm^2) as described in equation ***Ec. S3***. Finally, the Electrochemical Surface Area (ECSA)

was determined from the S_{CO}, the Pt-content catalytic load (L_{Pt} in µg cm^{-2} $_{geo}$), and the geometrical area of the RDE (A_{geo} in cm^2) as described in equation ***Ec. S4***

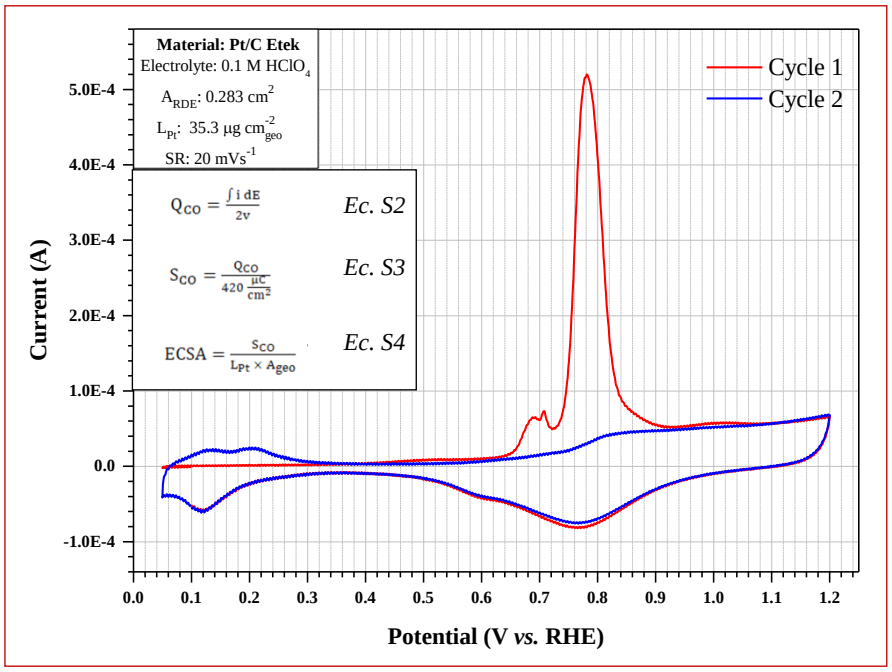

Figure S25. CO stripping obtained for the Pt/C Etek catalyst at 20 mV s^{-1} in a fresh 0.1M $HClO_4$ electrolyte solution after the activation procedure. The catalytic loading was L_{Pt} = 35.3 µg cm$^{-2}{}_{geo}$.

- ***Oxygen Reduction Reaction by steady-state polarization curves***

Measurements of the steady-state polarization curves were carried out to evaluate the activity toward the oxygen reduction reaction. CVs scans were performed at 20 mV s^{-1} in a potential window of 1.05 - 0.05 V *vs.* RHE, under O_2 saturation conditions of the 0.1 M $HClO_4$ electrolyte and with RDE or RRDE rotation rates aof 400, 900, 1600, and 2500 rpm (***Fig. S26***). The measurements began when a stable open circuit potential (OCP) was reached. For the calculations of catalytic activity, the subtraction of the N_2 background (previously measured in N_2 saturation conditions) from the polarization curves was conducted to suppress the capacitive effects of the catalyst material. The anodic sweep of the CV at 1600 rpm and normalized by the geometrical surface area of the electrode was considered for comparison between different materials.[3,4,10]

The polarization curves of all materials (with the exception of N-Oam100) were consistent with those corresponding to Pt-based catalysts; it was possible to distinguish *i)* the kinetic or activation control region (0.95 V *vs.* RHE < E <1.0 V *vs.* RHE) where the rate of the oxygen reduction is mainly controlled by a charge transfer process; *ii)* the mixed kinetic-diffusion control region (0.6 V *vs.* RHE < E < 0.95 V *vs.* RHE) where the rate of the reaction is simultaneously controlled by a mixed charge and mass process transfer; and *iii)* the diffusion control region (0.2 V *vs.* RHE < E < 0.6 V *vs.* RHE) where the constant limiting current density (J_l) depends only on a mass transport process (***Fig. S26***).[3,10,20]

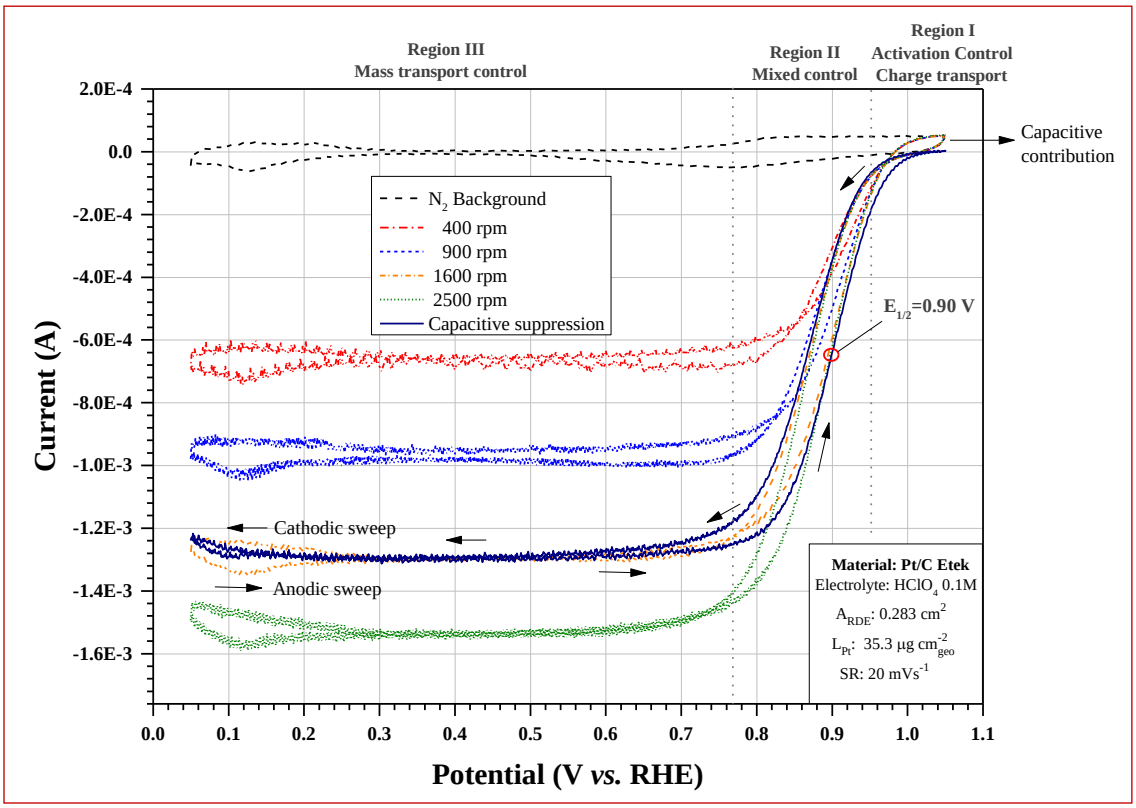

Figure S26. ORR steady-state polarization curves obtained for the Pt/C Etek catalyst at 20 mV s^{-1} and at different RDE rotation rates in a fresh 0.1M $HClO_4$ electrolyte solution saturated with O_2. The catalytic loading was L_{Pt} = 35.3 μg cm^{-2}_{geo}. Shown in the picture is the N_2 background voltammetry (black dashed line) and the polarization curve at 1600 rpm without the capacitive effect contribution (navy blue line) as obtained from the subtraction of the N_2 background voltammetry.

The Specific Activity (*SA* or j_k in mA cm^{-2}_{Pt}) and the Mass Activity (*MA* or j_m in A g^{-1}_{Pt}) kinetic parameters were respectively calculated from equations ***Ec. S5*** and ***Ec. S6***, where i_k is the kinetic current (A) obtained either graphically through the current intercept in the Koutecky-Levich plot at 0.9 V *vs.* RHE (***Fig. S27***), or by mass transport correction using the measured current (i) and the measured limiting current (i_l), as defined by the Levich equation (***Ec. S7***), where: *0.2* is a constant that is used when the RDE rotation rate is expressed in *rpm* (if it were given in angular frequency the constant would be *0.62 rad* s^{-1}); n = 4 is the number of electrons that are transferred for each oxygen diatomic molecule at the moment of reduction; F is Faraday's constant; A is the glassy carbon geometrical area of the W.E. in cm^2; D is the diffusion coefficient of oxygen in the electrolyte (1.7×10^{-5} cm^2 s^{-1} in 0.1M $HClO_4$); v is the kinematic viscosity of the electrolyte (1.01×10^{-2} cm^2 s^{-1} in 0.1M $HClO_4$); C is the concentration of oxygen dissolved in the electrolyte (1.26×10^{-6} mol cm^{-3} at a pressure of 1 atm); and ω is the speed of rotation of the electrode.[20–22]

$$j_k = i_k \times \frac{1}{S_{CO}} = \frac{i\ i_l}{i_l - i} \times \frac{1}{S_{CO}} \qquad \textit{Ec. S5}$$

$$j_m = j_k \times \frac{S_{CO}}{L_{Pt}\,A_{geo}} \qquad \textit{Ec. S6}$$

$$i_l = 0.2nFAD^{2/3}\nu^{-1/6}C\omega^{1/2} = B\omega^{1/2} \qquad \textit{Ec. S7}$$

Substituting the values of the constants in ***Ec. S7*** leads to the calculation of the Koutecky-Levich slope (*B*) which corresponded for Pt Etek to 13.83 × 10^{-2} mA cm^{-2} $rpm^{-0.5}$. However, it must not be omitted in equation ***Ec. S7*** that the dissolved oxygen concentration in the solution depends on the gas saturation pressure as a consequence of the atmospheric pressure. It is important to remember that O_2 concentration decreases with altitude. Thus, under the atmospheric conditions of this study (barometric pressure: 585 mmHg, and *ca.* 2300 m a.s.l), the electrochemical oxygen reduction experiments resulted in a lower *B* slope (11.54 × 10^{-2} mA cm^{-2} $rpm^{-0.5}$) (***Figure S27***). This is manifested by a lower experimental limiting current (approximately 4.62 mA cm^{-2} at 1600 rpm) which differs from other experimental values for the same Pt/C Etek catalyst (5.7 mA cm^{-2} at 1600 rpm) reported for O_2 saturation at altitudes close to sea level.[20,23,24] In other words, our experimental results present a 19% difference when compared to similar experiments performed at sea level; therefore, it is necessary to perform a correction to ensure comparability with those results found in literature. All numerical SA and MA parameters in this work were corrected by this factor.[24]

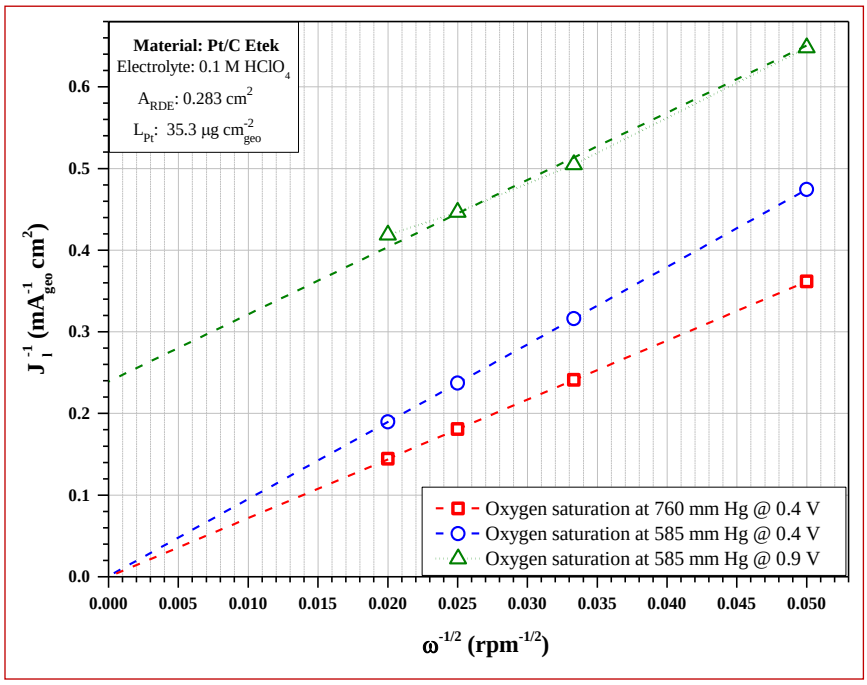

Figure S27. Koutecky-Levich slopes at different potentials obtained from ORR steady-state polarization curves measured at different RDE rotation rates for the Pt/C Etek catalyst. The catalytic loading was L_{Pt} = 35.3 µg cm^{-2}_{geo}. A comparison of the slopes at 0.4 V *vs.* RHE for the theoretical ORR measurements at 760 mmHg (red line) and the experimental results at 585 mmHg (blue line) is illustrated.

- ***Durability testing by accelerated electrochemical degradation***

Accelerated Electrochemical Degradation Testing (AEDT)[25–28] was performed to evaluate the durability of the best catalytic materials toward the ORR and of commercial Pt/C Etek. Testing consisted of 10,000 scans of cyclic voltammetry performed at a scan rate of 100 mV s^{-1} in a potential window of 0.6 - 1.0 V *vs.* RHE under O_2 saturation conditions. After completion of the 1000, 3000, 5000 and 10,000 cycles, an electrochemical evaluation protocol consisting of CV measurements under N_2 saturation, CO stripping, and ORR steady-state polarization curves with ohmic drop

compensation was implemented. SA and MA parameters corresponding to the degree of electrochemical degradation were determined and compared to each other.

- ***Determination of H_2O_2 formation by RRDE***

ORR can give rise to the formation of hydrogen peroxide if the reduction process is not carried out by a four-electron transfer. RRDE is a technique used to detect the reaction intermediaries to corroborate the preferred mechanism for ORR[7,20,22,29]. For this technique, steady-state curves were obtained for the material deposited on the glassy carbon of the W.E. using the bi-potentiostat mode that independently controls the potentials applied to the ring and the disk of the RRDE. During the measurement, the rotation of the electrode generates convection movements of the species in the solution, pushing them toward the surface of the disk where they become reduced by the applied potential. Then, the products generated in the disk are tangentially driven to the electrode ring where they are oxidized due to the applied potential of 1.55 V *vs*. RHE. The RRDE configuration permits for both the electrode disk and the collection ring to be kept in the same plane; however, not all the species generated in the disk reach the surface of the ring. Therefore, a collection factor (*N*) is required to determine the efficiency of the electrode (***Ec. S8***); this factor depends on the ring current (I_R) and the disk current (I_D). The collection factor N was calculated from the currents obtained from the polarization curves at different rotating rates using an aqueous solution composed of 10 mmol of $K_3Fe(CN)_6$ in 0.1 M $HClO_4$ as electrolyte (***Figure S28***).

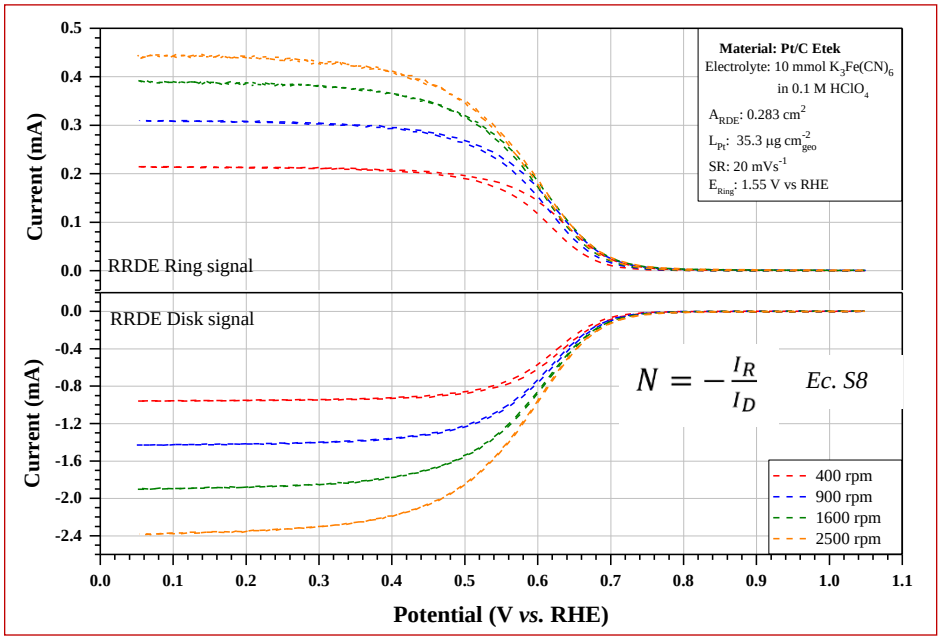

Figure S28. Polarization curves of the redox system Fe^{3+} / Fe^{2+} measured in the RRDE configuration.

During the analysis, a redox pair $Fe^{3+}(CN)_6^{3-}$ / $Fe^{2+}(CN)_6^{4-}$ was formed as a result of a reversible reaction from a one-electron transfer.[20] In the disk, a reduction process of Fe^{3+} is carried out to form Fe^{2+} species which are collected by the ring and oxidized into Fe^{3+}.

After the curves were obtained in the Potassium Ferricyanide, the electrolyte was replaced with a fresh $HClO_4$ solution to measure the polarization curves at different rotation rates in the bi-potentiostat mode. This test was applied

only to the synthesized Ni-Pt/VC material with the best catalytic activity and stability as compared to Pt/C Etek. The potential in the ring was fixed at 1.2 V *vs.* RHE. Disk and ring currents were inputted in Equation ***Ec. S9*** to determine the amount of H_2O_2 generated.[20] A low amount of peroxide formed (<5%) suggests that the kinetics for oxygen reduction are mostly carried out by a four-electron transfer which results in the formation of water.

$$X_{H_2O_2} = \frac{2I_R/N}{I_D + I_R/N} \qquad Ec.\ S9$$

SI-5. Membrane Electrode Assemblies (MEAs) preparation

- ***Catalytic ink preparation***

Catalytic inks of the best-performing synthetized Ni-Pt/VC (NP-Oam100) material and of Pt/C Etek catalyst were prepared by dispersion of the catalytic powders in a solution formulated with 2-propanol (*2P*), Nafion® perfluorinated resin solution (5 wt.% in lower aliphatic alcohols and water) (*N*), and 1-butanol (*B*). Inks were prepared using Pt/C Etek as the anodic catalyst, maintaining a Pt loading (L_{Pt}) of 0.02 mg cm^{-2}. For the cathode, the Ni-Pt/VC catalyst measured to obtain an L_{Pt} of 0.10 mg cm^{-2}. The volume percent of alcohols was 60 $_{v/v}$% of B and 40 $_{v/v}$% of 2P. Nafion solution content was calculated to have 30 wt.% of the solid resin with respect to the total catalyst content. After preparation, each ink was kept under magnetic stirring for 5 hours in chilled conditions.

- ***Catalytic ink impregnation on gas diffusion layer***

Commercial carbon cloth Gas Diffusion Layers (GDLs) were cut in squares of 2.2 × 2.2 cm (5 cm^2) and placed on a hot-plate at 60°C. Anodic and cathodic catalytic inks were separately impregnated on the carbon surface of the GDLs by a paintbrush technique. GDLs were rotated 90° before applying a new coat of ink in order ensure uniformity. A GDL which contains a catalytic material is known as a Gas Diffusion Catalyst (GDC). After catalytic deposit, GDCs were dried inside an oven at 120 °C to evaporate the solvents.

- ***Preparation of MEAs***

Membrane electrode assemblies were prepared by a hot-pressing technique using a GDC with Pt/C Etek (L_{Pt}: 0.02 mg cm^{-2}) as anode and a GDC with Ni-Pt/VC (L_{Pt}: 0.10 mg cm^{-2}) as cathode. A commercial Nafion® NR-212 membrane was used as received and without further activation as a polymer electrolyte. The assembly was placed between two stainless-steel sheets heated at 120 °C and pressed in a hydraulic press applying a rate of 40 kg per cm^{-2} (considering the surface area of the GDC) for 120 seconds. Optimized time, temperature, and pressure parameters have been reported in existing literature.[30–34]

SI-6. Single-Fuel cell performance evaluation details

MEAs performance evaluation was carried out in a Fuel Cell Test System model 890B coupled to a Compucell GT humidification system. A single fuel cell model ElectroChem EFC-25-04 was used during performance evaluation. The humidification temperature of the gases was fixed at 80 °C for both anode (T_{ha}) and cathode (T_{hc}), and the cell temperature (T_{cell}) was set at 85 °C. The anodic flow (F_a) was fixed at 120 cm^3 min^{-1} of hydrogen and the cathodic flow (F_c) at 100 cm^3 min^{-1} of oxygen. The backup pressure both anodic and cathodic sides was set to 30 PSI.

Membrane electrode assemblies must undergo to an activation process (like the one carried out during electrochemical cell evaluations) prior to the evaluation of the polarization curves in order to ensure that the maximum performance of the catalytic materials is obtained. The choice of the appropriate activation protocol constitutes an optimizable process where many variables are involved. Existing literature reports many activation protocols based on prolonged potential or current steps [35–37]. The protocol used in this work was developed taking as reference the procedures established by the U.S. Department of Energy (*DoE*).[38,39] ***Table S5*** shows the potential steps of the implemented activation protocol. ***Figure S30*** shows the profile of the activation protocol over time.

Table S5. Activation protocol for MEAs performance evaluation.

Potential (V)	Time (min)	Step
0.4	2	Current density monitoring
0.6	60	Stage I – Membrane hydration
0.4	2	Current density monitoring
0.7	20	Stage II – Catalysts activation (these steps are repeated n times)
0.5	20	
0.4	2	Current density monitoring

As the activation protocol is running, it is possible to observe changes in the current. Stage II of the protocol, where the catalyst activation is carried out under potential steps between 0.7 and 0.5 V is repeated for several cycles until the current between two consecutive cycles was very similar or when difference did not exceed 5% (***Figure S31***). When this condition was fulfilled, the activation protocol was concluded.

After activation, the polarization curves were obtained through a potential sweep from the Open Circuit Voltage of cell (OCV) to 0.3 V. The product of the cell voltage with the current density gives the power density curves.

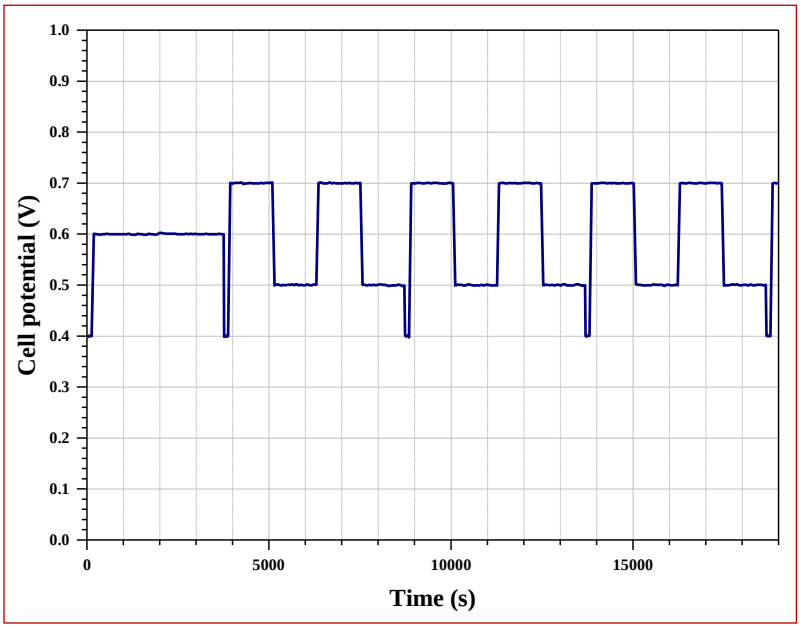

Figure S30. Potential steps during the activation protocol.

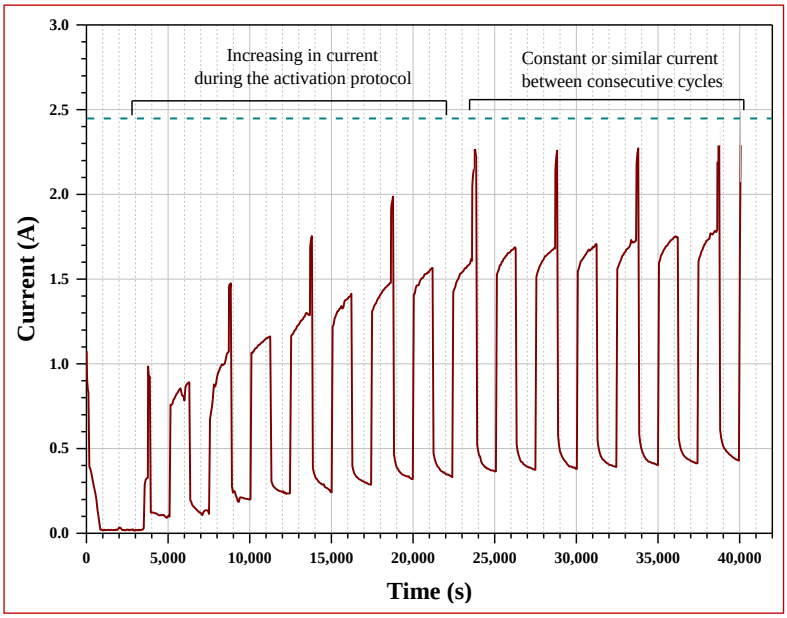

Figure S31. Evolution of the current during the activation protocol.

SI-7. Construction and performance evaluation details of a low-power PEM fuel cell prototype

A low power fuel cell prototype consisting of six single-cells was built. Its design was carried out by AutoCAD software, taking into account different designs proposed in the literature.[40–42] Monopolar, bipolar (***Figure S32***), and end plates were manufactured using a CNC milling machine model EMCO Concept Mill 55. Gaskets, membranes and acrylic pieces were cut by a Golden Laser precision laser cutter.

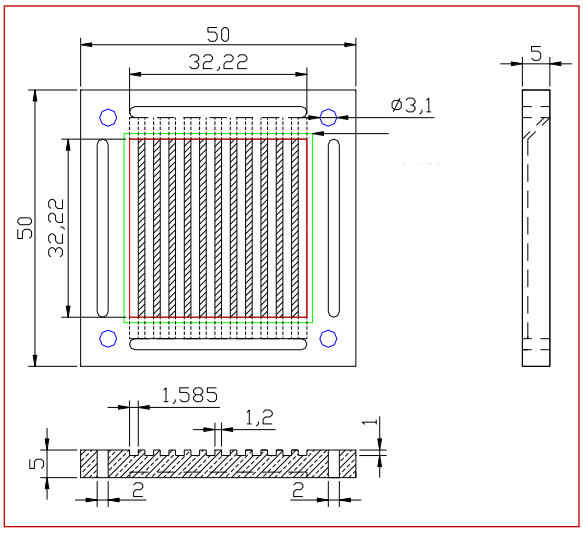

Figure S32. Dimensions of the bipolar graphite plate of one of the single-cells of the prototype.

Fuel cell prototype was constituted by high-density graphite plates (50 mm square side) with a thickness of 5 mm. The field-flow design for gas either anode and cathode were in a parallel arrangement, designed to have channels of 1.58 mm wide and 1 mm deep. Two brass sheets act as current collectors and two acrylic plates as input and output chambers for hydrogen and oxygen. Aluminum end plates were used to secure the stack structure with stainless steel studs and nuts (***Figure S33-a***). Between each bipolar plate there is a membrane-electrode assembly (MEA) insulated by silicone gaskets (thickness: 0.38 mm).

Catalytic inks were prepared with the same procedure as was described before using Pt/C Etek (L_{Pt}: 0.02 mg cm^{-2}) as anode and Ni-Pt/VC (L_{Pt}: 0.10 mg cm^{-2}) as cathode. Inks were impregnated onto the GDL's (9 cm^2) and the MEAs were prepared by hot-pressing using Nafion® NR-212 membranes. The resulting assembly of a low-power fuel cell prototype is shown (***Figure S33-b-c***).

The prototype was evaluated in the fuel cell testing system. The working conditions were: humidification temperature fixed at 80 °C, cell at room temperature, backup pressures at 7 PSI, and gas flows of 120 cm^3 min^{-1} for anode and cathode. During the operation the cell reached a temperature of 34 °C.

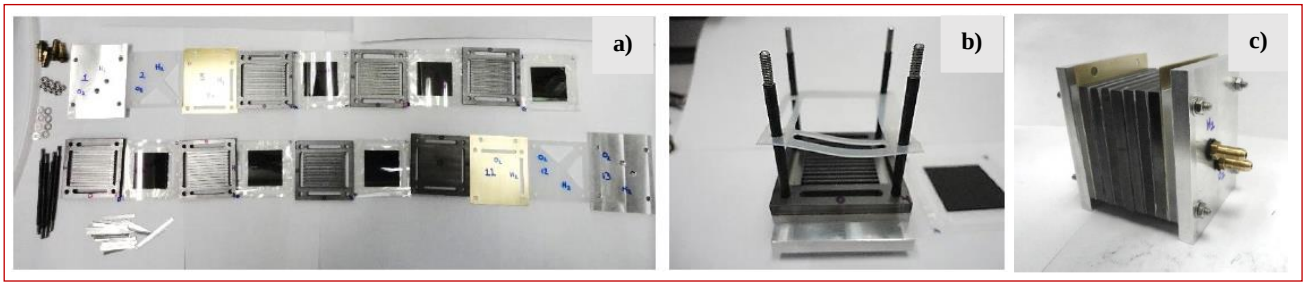

Figure S33. a) Components for the low-power fuel cell prototype, **b)** components assembling, and **c)** final prototype.

References

1 W. Bu, Z. Chen, F. Chen and J. Shi, *J. Phys. Chem. C*, 2009, **113**, 12176–12185.

2 J. L. Reyes-Rodríguez, D. Bahena-Uribe, J. Roque, A. Velázquez-Osorio and O. Solorza-Feria, *MRS Commun.*, 2017, **7**, 947–952.

3 Y. Garsany, O. a Baturina, K. E. Swider-Lyons and S. S. Kocha, *Anal. Chem.*, 2010, **82**, 6321–6328.

4 K. Shinozaki, J. W. Zack, R. M. Richards, B. S. Pivovar and S. S. Kocha, *J. Electrochem. Soc.*, 2015, **162**, 1144–1158.

5 N. Hodnik, C. Baldizzone, S. Cherevko, A. Zeradjanin and K. J. J. Mayrhofer, *Electrocatalysis*, 2015, **6**, 237–241.

6 D. Van Der Vliet, D. S. Strmcnik, C. Wang, V. R. Stamenkovic, N. M. Markovic, M. T. M. Koper, D. Van Der Vliet, D. S. Strmcnik, C. Wang, V. R. Stamenkovic, N. M. Markovic and M. T. M. Koper, *J. Electroanal. Chem.*, 2010, **647**, 29–34.

7 J. L. Reyes-Rodríguez, F. Godínez-Salomón, M. A. Leyva and O. Solorza-Feria, *Int. J. Hydrogen Energy*, , DOI:10.1016/j.ijhydene.2012.12.031.

8 J. Clavilier, J. M. Orts, R. Gómez, J. M. Feliu and A. Aldaz, *J. Electroanal. Chem.*, 1996, **404**, 281–289.

9 T. J. Schmidt, H. a Gasteiger, G. D. Stab, P. M. Urban, D. M. Kolb and R. J. Behm, *J. Electrochem. Soc.*, 1998, **145**, 2354–2358.

10 K. J. J. Mayrhofer, D. Strmcnik, B. B. Blizanac, V. Stamenkovic, M. Arenz and N. M. Markovic, *Electrochim. Acta*, 2008, **53**, 3181–3188.

11 M. Arenz, K. J. J. Mayrhofer, V. Stamenkovic, B. B. Blizanac, T. Tomoyuki, P. N. Ross and N. M. Markovic, *J. Am. Chem. Soc.*, 2005, **127**, 6819–6829.

12 U. a. Paulus, a. Wokaun, G. G. Scherer, T. J. Schmidt, V. Stamenkovic, N. M. Markovic and P. N. Ross, *Electrochim. Acta*, 2002, **47**, 3787–3798.

13 T. J. Schmidt, *J. Electrochem. Soc.*, 1998, **145**, 2354.

14 P. Ochal, J. L. Gomez de la Fuente, M. Tsypkin, F. Seland, S. Sunde, N. Muthuswamy, M. Rønning, D. Chen, S. Garcia, S. Alayoglu and B. Eichhorn, *J. Electroanal. Chem.*, 2011, **655**, 140–146.

15 F. Maillard, M. Eikerling, O. V Cherstiouk, S. Schreier, E. Savinova and U. Stimming, *Faraday Discuss.*, 2004, **125**, 357–377.

16 S. Brimaud, S. Pronier, C. Coutanceau and J. M. Léger, *Electrochem. commun.*, 2008, **10**, 1703–1707.

17 K. J. J. Mayrhofer, M. Arenz, B. B. Blizanac, V. Stamenkovic, P. N. Ross and N. M. Markovic, *Electrochim. Acta*, 2005, **50**, 5144–5154.

18 S. Kinge, C. Urgeghe, A. De Battisti and H. Bönnemann, *Appl. Organomet. Chem.*, 2008, **22**, 49–54.

19 T. Vidaković, M. Christov and K. Sundmacher, *Electrochim. Acta*, 2007, **52**, 5606–5613.

20 U. a. Paulus, T. J. Schmidt, H. A. Gasteiger and R. J. Behm, *J. Electroanal. Chem.*, 2001, **495**, 134–145.

21 D.-S. Yang, M.-S. Kim, M. Y. Song and J.-S. Yu, *Int. J. Hydrogen Energy*, 2012, **37**, 13681–13688.

22 T. J. Schmidt, U. a. Paulus, H. a. Gasteiger and R. J. Behm, *J. Electroanal. Chem.*, 2001, **508**, 41–47.

23 S. C. Perry and G. Denuault, *Phys. Chem. Chem. Phys.*, 2015, **17**, 30005–30012.

24 E. Teran-Salgado, D. Bahena-Uribe, A. M. Pedro, J. L. Reyes-Rodriguez, R. Cruz-Silva and O. Solorza-Feria, *Electrochim. Acta*, 2019, **298**, 172–185.

25 X. Wang, L. Figueroa-Cosme, X. Yang, M. Luo, J. Liu, Z. Xie and Y. Xia, *Nano Lett.*, 2016, **16**, 1467–1471.

26 H. R. Colón-Mercado, H. Kim and B. N. Popov, *Electrochem. commun.*, 2004, **6**, 795–799.

27 J. H. Kim, J. Y. Cheon, T. J. Shin, J. Y. Park and S. H. Joo, *Carbon N. Y.*, 2016, **101**, 449–457.

28 Y. Li, Y. Li, E. Zhu, T. McLouth, C.-Y. Chiu, X. Huang and Y. Huang, *J. Am. Chem. Soc.*, 2012, **134**, 12326–12329.

29 N. M. Markovic, T. J. Schmidt, V. Stamenkovic and P. N. Ross, *Fuel Cells*, 2001, **1**, 105–116.

30 A. Therdthianwong, P. Manomayidthikarn and S. Therdthianwong, *Energy*, 2007, **32**, 2401–2411.

31 S. Martemianov, V. a. Raileanu Ilie and C. Coutanceau, *J. Solid State Electrochem.*, 2014, **18**, 1261–1269.

32 M. Yazdanpour, A. Esmaeilifar and S. Rowshanzamir, *Int. J. Hydrogen Energy*, 2012, **37**, 11290–11298.

33 O. Okur, Ç. İyigün Karadağ, F. G. Boyacı San, E. Okumuş and G. Behmenyar, *Energy*, 2013, **57**, 574–580.

34 K. S. Loh, a. B. Mohamad, N. Harahap, a. a. H. Kadhum and W. R. W. Daud, *Chem. Eng. Technol.*, 2011, **34**, 439–444.

35 M. Boaventura and a. Mendes, *Int. J. Hydrogen Energy*, 2010, **35**, 11649–11660.

36 C. Yang, M. Hu, C. Wang and G. Cao, *J. Power Sources*, 2012, **197**, 180–185.

37 Z. Qi and A. Kaufman, *J. Power Sources*, 2003, **114**, 21–31.

38 U.S. Department of Energy, 2009, 70.

39 U. Fuel Cell Council, *USFCC Single Cell Test Protocol # 05-014*, Washington DC, 2006.

40 F. Urbani, G. Squadrito, O. Barbera, G. Giacoppo, E. Passalacqua and O. Zerbinati, 2007, **169**, 334–337.

41 X. Li and I. Sabir, 2005, **30**, 359–371.

42 F. Barbir, *PEM Fuel Cells: Theory and Practice*, Elsevier Academic Press, 2nd edn., 2012.